



1 **Observations of traveling ionospheric disturbances driven by gravity waves from sources**
2 **in the upper and lower atmosphere**
3
4

5 Paul Prikryl¹, David R. Themens^{1,2}, Jaroslav Chum³, Shibaji Chakraborty⁴, Robert G. Gillies⁵,
6 James M. Weyand⁶
7

8 ¹Physics Department, University of New Brunswick, Fredericton, NB, Canada

9 ²School of Engineering, University of Birmingham, Birmingham, UK

10 ³Institute of Atmospheric Physics CAS, Prague, Czech Republic

11 ⁴Center for Space Science and Engineering Research, Virginia Tech, Blacksburg, VA, USA

12 ⁵Department of Physics and Astronomy, University of Calgary, Calgary, AB, Canada

13 ⁶Earth, Planetary, and Space Sciences, University of California, Los Angeles, CA, USA
14
15
16

17 *Correspondence to:* Paul Prikryl (paul.prikryl@unb.ca)

18
19
20 **Abstract**

21 Traveling ionospheric disturbances (TIDs) are observed by the Super Dual Auroral Radar Network
22 (SuperDARN), the Poker Flat Incoherent Scatter Radar (PFISR), the multipoint and
23 multifrequency continuous Doppler sounders, and the GNSS total electron content (TEC) mapping
24 technique. PFISR measures electron density altitude profiles, from which TIDs are obtained by a
25 filtering method to remove background densities. SuperDARN observes the ionospheric
26 convection at high latitudes and TIDs modulating the ground scatter power. The Doppler sounders
27 at mid latitudes can determine TID propagation velocities and azimuths. The aim of this study is
28 to attribute the observed TIDs to atmospheric gravity waves generated in the lower thermosphere
29 at high latitudes, or gravity waves generated by mid-latitude tropospheric weather systems. The
30 solar wind-magnetosphere-ionosphere-thermosphere coupling modulates the dayside ionospheric
31 convection and currents that generate gravity waves driving equatorward propagating medium to
32 large scale TIDs. The horizontal equivalent ionospheric currents are estimated from the ground-
33 based magnetometer data using an inversion technique. At high latitudes, TIDs observed in the
34 detrended TEC maps are dominated by equatorward TIDs pointing to auroral sources. At mid to
35 low latitudes, the azimuths of TIDs vary, indicating sources in the troposphere. The cases of
36 eastward to southeastward propagating TIDs that are observed in the detrended TEC maps and by
37 the HF Doppler sounders in Czechia are attributed to gravity waves that were likely generated by
38 geostrophic adjustment processes and shear instability in the intensifying low-pressure systems.



39 1. Introduction

40 The relationship between atmospheric gravity waves (AGWs) and traveling ionospheric
41 disturbances (TIDs) has been well established (Hocke and Schlegel, 1996). The theory governing
42 the propagation and effects of AGWs in the ionosphere was developed by Hines (1960) and their
43 ionospheric sources have been recognized (Chimonas, 1970; Chimonas and Hines, 1970; Testud,
44 1970; Richmond, 1978). Global propagation of medium- to large-scale GWs/TIDs has been linked
45 to auroral sources (Hunsucker, 1982; Hajkowicz, 1991; Lewis *et al.*, 1996; Balthazor and J., 1997).
46 The Worldwide Atmospheric Gravity-wave Studies (WAGS) program (Crowley and Williams,
47 1988; Williams *et al.*, 1993) showed that large-scale TIDs originate in auroral latitudes. TIDs
48 generated by AGWs originating in the lower atmosphere come from a variety of sources, including
49 tropospheric weather systems (Bertin, Testud and Kersley, 1975; Bertin *et al.*, 1978; Waldoock and
50 Jones, 1987; Oliver *et al.*, 1997; Nishioka *et al.*, 2013; Azeem *et al.*, 2015), total solar eclipses
51 (Zhang *et al.*, 2017; Mrak *et al.*, 2018), the polar vortex (Frissell *et al.*, 2016), volcanic eruptions,
52 earthquakes, and tsunamis (Yu, Wang and Hickey, 2017; Nishitani *et al.*, 2019; Themens *et al.*,
53 2022).

54
55 The solar wind coupling to the dayside magnetosphere (Dungey, 1961, 1995) generates variable
56 electric fields that map to the ionosphere driving the $E \times B$ ionospheric convection and
57 currents. The Joule heating due to the ionospheric currents of in the lower thermosphere is a source
58 of equatorward propagating AGWs, which in turn drive TIDs (e.g., Prikryl *et al.*, 2022). The
59 electric fields transmitted to the low latitude ionosphere in the magnetosphere-ionosphere current
60 circuit (Kikuchi and Hashimoto, 2016) play a role in generating TIDs through ion-neutral
61 interactions (Nishitani *et al.*, 2019) and an electrodynamic instability mechanism (Kelley *et al.*,
62 2023). In the troposphere, convection is often a source of gravity waves propagating into the upper
63 atmosphere driving TIDs (e.g., Azeem, 2021; and references therein). However, large amplitude
64 gravity waves generated in the troposphere by geostrophic adjustment processes and shear
65 instability (Klostermeyer, 1977; Uccellini and Koch, 1987) have been rarely considered to drive
66 TIDs.

67

68 We present observations of TIDs by radars, Doppler sounders and the GNSS TEC mapping
69 technique. The aim of this study is to attribute the observed TIDs to sources in the upper (Section



70 3), and the lower (Section 4) atmosphere. These observations show that AGWs provide both
71 downward and upward vertical coupling of the ionosphere and neutral atmosphere.

72

73 **2. Data sources and methods**

74 Advanced Modular Incoherent Scatter Radar (AMISR) technology with its unique steering and
75 beam-forming capabilities has been described by Heinselman and Nicolls (2008) and has been
76 used to investigate gravity wave propagation (Nicolls and Heinselman, 2007; Vadas and Nicolls,
77 2008). The Poker Flat Incoherent Scatter Radar (PFISR) located at the Poker Flat Research Range
78 (65.1°N, 147.5°W) near Fairbanks, Alaska running a 7-beam mode (Heinselman and Nicolls,
79 2008) measured altitude profiles of the electron densities. To retrieve TIDs, background densities
80 are removed by applying Savitzky-Golay filter (Press and Teukolsky, 1990).

81

82 The multi-point and multi-frequency continuous HF Doppler sounding system operating in the
83 Czech Republic is described by Chum et al. (2021). It consists of three transmitting sites Tx1,
84 Tx2, and Tx3 distributed in the western part of the Czech Republic (Tx1: 50.528°N, 14.567°E;
85 Tx2: 49.991°N, 14.538°E; Tx3: 50.648°N, 13.656°E) and receiver Rx located in Prague
86 (50.041°N, 14.477°E). Radio waves at different frequencies (3.59, 4.65 and 7.05 MHz) are
87 transmitted from each site. First, the time evolution of power spectral densities (Doppler shift
88 spectrograms) are computed for each signal and the maximum of power spectral density
89 (characteristic Doppler shift) is found with selected time resolution suitable for the TIDs/GWs
90 analysis (30 or 60 s). TID/GW cause movement of plasma and therefore the Doppler shift. The
91 propagation velocities and azimuths are then determined from the time delays between the Doppler
92 shifts recorded for different transmitter-receiver pairs and expected distances of the reflection
93 points in the ionosphere are determined by two- or three- dimensional methods described in detail
94 by Chum and Podolská (2018) and Chum et al. (2021).

95

96 SuperDARN constitutes a globally distributed HF Doppler radar network, operational within the
97 frequency range of 8 to 18 MHz, encompassing both the northern and southern hemispheres across
98 various latitudinal bands, including middle, high, and polar zones. Each radar within this network
99 measures the line-of-sight (LoS) component of the drift velocity associated with ionospheric
100 plasma irregularities (Chisham et al., 2007; Nishitani et al., 2019). The observations from



101 SuperDARN encompass two principal forms of backscatter, namely, ionospheric scatter and
102 ground scatter. Ionospheric scatter is generated when a transmitted signal is scattered from
103 ionospheric irregularities. In the case of ground scatter, due to the significant daytime vertical
104 refractive index gradient, the propagation rays alter their trajectory towards the ground, scattering
105 from surface roughness before returning along the same path to the radar. Prior research has
106 demonstrated the utility of both scatter types in studies of pulsed ionospheric flows (PIFs)
107 (McWilliams, Yeoman and Provan, 2000; Prikryl *et al.*, 2002) and TIDs (Samson *et al.*, 1990). In
108 this study, we use line-of-sight (LoS) Doppler velocities and ground scatter observations to
109 characterize TIDs, with supplementary support from ionospheric convection maps available at the
110 SuperDARN Virginia Tech (VT) website (vt.superdarn.org) to validate their sources.

111

112 The Spherical Elementary Current System (SECS) inversion technique (Amm and Viljanen, 1999)
113 is used to estimate horizontal equivalent ionospheric currents (EICs) from the ground-based
114 magnetic field measurements by several arrays of magnetometers in the North American sector
115 and the western Greenland (Weygand *et al.*, 2011; their Table 1). For each of these magnetometers
116 the quiet-time background is subtracted from the measured field to give the disturbance component
117 which determines the EICs (Weygand *et al.*, 2011).

118

119 Global Navigation Satellite System (GNSS) data for this were gathered from the same global
120 networks of GNSS receivers used in Themens *et al.* (2022), which constitute 5200-5800 stations,
121 depending on the period. Examples of the GNSS station distribution in the two local domains can
122 be viewed in Fig. S1 in the Supplement. Using the phase leveling and cycle slip correction method
123 outlined by Themens *et al.* (2013), the LoS total electron content (TEC) is determined from the
124 differential phase and code measurements of these systems. As detailed in Themens *et al.* (2015),
125 the satellite biases are acquired from the Center for Orbit Determination in Europe (CODE,
126 <ftp://ftp.aiub.unibe.ch/>) and receiver biases are determined.

127

128 To characterize the TID structures using these data, LoS TEC measurements for each satellite-
129 receiver pair were detrended by first projecting the LoS TEC to vertical TEC (vTEC) using the
130 thin shell approximation at 350-km altitude and subtracting the sliding 60-minute average. More



131 details on this method can be found in Themens et al. (2022). The TEC anomalies are then binned
132 in 0.75-degree latitude and longitude bins for mapping.

133

134 The Goddard Space Flight Center Space Physics Data Facility
135 (<https://spdf.gsfc.nasa.gov/index.html>) and the National Space Science Data Center OMNIWeb
136 (<http://omniweb.gsfc.nasa.gov>) (King and Papitashvili, 2005) archive the solar wind data. The
137 magnetic field measurements obtained by Advanced Composition Explorer (ACE) (Smith *et al.*,
138 1998) are used.

139

140 **3. AGWs/TIDs originating from lower thermosphere at high latitudes**

141

142 van de Kamp et al. (2014) described two techniques to detect TIDs, one using the EISCAT
143 incoherent scatter radar near Tromsø, and the other using the detrended GPS TEC data. They
144 determined parameters characterizing TIDs and studied an event of January 20, 2010. While these
145 authors did not investigate the origin of the TIDs they suggested that the AGWs were most likely
146 generated at low atmospheric layers. Using the EISCAT Svalbard radars on February 13, 2001,
147 Cai et al. (2011) observed moderately large-scale TIDs propagating over the dayside polar cap that
148 were generated by the nightside auroral heating. It is noted that both these TID events occurred on
149 days following arrivals of corotating interaction regions (CIRs) at the leading edge of solar wind
150 high-speed streams that can trigger moderate geomagnetic storms (Tsurutani et al., 1990, 2006).

151

152 Frissell et al. (2016) concluded that polar atmospheric processes, namely the polar vortex, rather
153 than space weather activity are primarily responsible for controlling the occurrence of high-latitude
154 and midlatitude winter daytime medium-scale TIDs (MSTIDs). This paper has been frequently
155 cited to justify suggestions of polar vortex as a source of the observed MSTIDs (Bossert et al.,
156 2021; Becker et al., 2022; Goncharenko et al., 2022). Bossert et al. (2021) studied gravity waves
157 generated by stratospheric vortex on January 8, 2013, which they suggested had caused TIDs
158 observed by PFISR in Poker Flat, Alaska. In Section 3.1, we examine this event in the context of
159 solar wind coupling to show evidence that the observed TIDs originated in the high-latitude
160 dayside ionosphere poleward of Alaska.

161



162 In Section 3.2, we present observations of TIDs generated by solar wind-M-I-T coupling on the
163 dayside following the arrival of high-speed streams (HSSs) permeated by solar wind Alfvén waves
164 (Belcher and Davis, 1971; Tsurutani et al., 1987). Solar wind Alfvén waves can modulate
165 ionospheric convection and currents producing polar cap density patches and TIDs (Prikryl *et al.*,
166 1999, 2005, 2022).

167

168 3.1. Event of January 8/9, 2013

169 In the period from January 8 to 15 the PFISR beams scanned electron densities, N_e (cm^{-3}), at
170 altitudes from 150 to 500 km. In the detrended TEC maps over Alaska ([https://acr-nc-](https://acr-nc-web.nict.go.jp/GPS/GLOBAL/MAP/2013/008/index.html)
171 [web.nict.go.jp/GPS/GLOBAL/MAP/2013/008/index.html](https://acr-nc-web.nict.go.jp/GPS/GLOBAL/MAP/2013/008/index.html)) the equatorward propagating TIDs
172 were observed on each day during the daytime hours when the PFISR density data show signatures
173 of downward propagating phase of TIDs. Fig. 1a shows N_e in logarithmic scale as a function of
174 altitude observed by the radar beam 2 at temporal resolution of 3 min between 18:00 and 03:00
175 UT (09:00 and 18:00 LT) on January 8-9, 2013. The downward propagating phase of TIDs is
176 readily seen superposed on the background of high daytime densities. To remove the background
177 and highlight the TIDs with periods > 40 min the time series for each altitude are detrended using
178 a 33-point wide Savitzky-Golay filter (4th degree, 2nd order) (Fig. 1b). To show the equatorward
179 propagation of the TIDs across Alaska, Fig. 1c shows the detrended GNSS νTEC mapped at
180 latitude bins along the longitude of the PFISR.

181

182 Bossert et al. (2021) argued that because this event occurred during a geomagnetically quiet period,
183 other than auroral sources should be considered for the observed TIDs, namely, the polar vortex.
184 The geomagnetic activity on January 8 was low, with the Kp -index ≤ 1 except for a peak of 3- in
185 the last 3-hourly interval caused by a substorm that occurred in the European sector. The
186 northernmost magnetometer in Alaska in Barrow observed the north-south X -component magnetic
187 field perturbation of ~ 230 nT at 17:10 UT (see Fig. S2 in the Supplement) indicating the westward
188 electrojet. At this time, the IMF was pointing downward ($B_y < 0$) and eastward flows (see Fig. S3a
189 in the Supplement) in the dawn convection cell corresponded with the westward electrojet sensed
190 in Barrow. After 18:00 UT, as the IMF B_y reversed to duskward (Figure 2c), the convection cells
191 receded further poleward of Alaska and the convection pattern become dominated by the dusk cell



192 (see Fig. S3b in the Supplement). At this time, the distant westward electrojet over Beaufort Sea
193 could no longer be detected by magnetometers.

194

195 The King Salmon Radar (KSR) beam 9 pointing northwest over the East Siberian Sea observed
196 positive (towards the radar) line-of-sight (LoS) velocities indicating quasiperiodic (20-50 min)
197 pulsed ionospheric flows (PIFs; Fig. 2a) in the dawn convection cell. At near ranges, the KSR
198 radar observed enhancements in the sea scatter power (Fig. 2b) caused by a series of equatorward
199 propagating TIDs. The Prince George Radar (PGR) beam 1 also observed the TIDs in the ground
200 scatter power (Fig. 2d). The periodicities of these TIDs were similar to those of PIFs and the TIDs
201 observed by PFISR (Fig. 2c).

202

203 The IMF southward turnings are expected to result in enhanced reconnection rate leading to
204 intensifications of the ionospheric convection/currents in the cusp footprint that were sources of
205 TIDs. One of the convection enhancements can be viewed in Fig. S3b in the Supplement. The time
206 series of the ACE IMF B_y and B_z , as well as the clock angle counted from the geomagnetic north,
207 with the 180° (dotted line) indicating southward turnings of the IMF are shown time-shifted in Fig.
208 2c. The clock angle controls the reconnection rate at the magnetopause (Milan et al., 2012). The
209 TIDs can be approximately associated with southward IMF turnings (positive deflections of the
210 clock angle values towards 180° marked by arrows in Fig. 2).

211

212 This assessment provides evidence that the observed TIDs could have originated from the
213 magnetosphere/solar wind forcing rather than due to lower-atmospheric forcing. This highlights
214 the significant challenge that exists in clearly identifying the source of TIDs in ionospheric
215 observations and shows that a broad range of factors need to be considered together when
216 attributing TID sources.

217

218 While we focused here on January 8/9, on each day during the PFISR experiment from January 8
219 to 15 the solar wind-MIT coupling that modulated PIFs in the ionospheric cusp footprint poleward
220 of Alaska launched TIDs that were observed by PFISR, as well as in the GNSS $vTEC$ maps.
221 Similarly, in the European sector, dayside TIDs propagating equatorward from their sources in the
222 cusp over Svalbard were also observed. This can be viewed in Fig. S4 in the Supplement.



223

224 *3.2. Events of November 1 and 4-5, 2014*

225 Solar wind Alfvén waves permeate HSSs, and along with CIRs, are highly geoeffective when IMF
226 $B_z < 0$ (Tsurutani et al., 1987, 1995, 2006). Following arrivals of HSS/CIRs (marked by asterisks
227 in Fig. 3) on November 1 and 5, 2014, the solar wind Alfvén waves are characterized by the Walén
228 relation between velocity V and magnetic field B (Yang, Chao and Lee, 2020). The components of
229 the corresponding components of the magnetic field (B_y and B_z) and velocity (V_y and V_z) observed
230 by ACE are correlated (Fig. 4a), a signature of solar wind Alfvén waves.

231

232 In the European sector, the SuperDARN Hankasalmi radar observed PIFs in the cusp over Svalbard
233 and equatorward propagating TIDs that were also observed in the detrended vTEC. Figs. 5 and 6
234 show the ionospheric LoS velocities and the radar scatter power (ground scatter shown in grey
235 color in the velocity plot) observed by the radar beam 11 on November 1 and 5, respectively. The
236 ground magnetic field perturbations of the X-component observed in Ny Ålesund (NAL;
237 <https://space.fmi.fi/image/www/index.php>) are superposed. The radar observed a series of
238 intensifications of the negative (away from the radar) LoS velocities (PIFs) at ranges greater than
239 ~ 2000 km on the dayside, starting at $\sim 07:00$ UT with the onset of ionospheric currents fluctuations
240 sensed by the NAL magnetometer. The solar wind Alfvén waves modulated the dayside
241 ionospheric currents launching AGWs driving the equatorward propagating TIDs observed in the
242 radar ground scatter at ranges below ~ 2000 km. For the first event, Figs. 4b and 4c show the FFT
243 spectra of detrended time series of IMF B_z , solar velocity V_z , the NAL X-component, and the
244 Hankasalmi radar ground scatter power displaying peaks at similar frequencies/periods.

245

246 Figs. 7a and 7b show the TIDs observed in the detrended vTEC as alternating positive and negative
247 anomalies mapped along longitude of 15°E on November 1 and 5, respectively. The equatorward
248 TIDs were observed at least down to latitude of 50°N , where the equatorward motion appears to
249 be disrupted due to interference with TIDs from tropospheric sources moving eastward to
250 southeastward that are discussed in Section 4.

251

252 The arrival of the HSS/CIR on November 4 triggered a minor geomagnetic storm with the Dst
253 index reaching maximum negative value of -44 nT (Fig. 3) (Gonzalez *et al.*, 1994). Similar to



254 cases reported previously (Prikryl et al., 2022), intense ionospheric currents in the North American
255 sector auroral zone launched large-scale TIDs (LSTIDs) that were observed by the midlatitude
256 SuperDARN radars and the detrended TEC. Before 4:00 UT at radar frequency at 11.5 MHz, the
257 Fort Hays West (FHW) midlatitude radar beam 12 looking northwest over the central Canada
258 observed the ionospheric scatter showing enhancements in the positive LoS velocities (toward the
259 radar; Fig. 8a) due to fluctuating eastward ionospheric flows at the equatorward edge of an
260 expanded dawn convection cell associated with the fluctuating westward electrojet. The
261 ionospheric currents were sensed by magnetometers, including one in Fort Simpson (FSIM;
262 www.carisma.ca/). The X component of the ground magnetic field and time series of the latitudinal
263 maxima in EICs at the longitude of 120°W, are superposed. After 14:00 UT, when the radar
264 frequency was set to 15 MHz, the HF propagation allowed to observe TIDs in the ground scatter.
265 Instead of the slant range, to reflect the actual TID location in the ionosphere, the ground-scatter
266 range mapping (Bristow, Greenwald and Samson, 1994; Frissell *et al.*, 2014) can be applied. In
267 this case, the slant ranges between 1000 and 3000 km correspond to the mapped ground scatter
268 range between 200 and 1200 km.

269

270 Two major intensifications of the westward electrojet at ~13:10 and 14:10 UT launched LSTIDs
271 observed in the ground scatter starting at ~14:00 and 15:00 UT (Fig. 8b). The mapped EICs in
272 Fig. 9a show the first major intensification of the westward electrojet (the EIC maxima at each
273 longitude are highlighted). It launched an equatorward propagating LSTID observed in the
274 detrended v TEC maps (Fig. 9b). The second intensification of the westward electrojet launched
275 another LSTID observed in the radar ground scatter starting at ~15:00 UT (Fig. 8b), as well as in
276 the detrended v TEC. Figs. 10a and 10b show the LSTIDs observed in the detrended v TEC mapped
277 along longitude of 100°W and 15°E, respectively. In the North American sector, the LSTIDs were
278 observed between 13:00 and 16:00 UT (Fig. 10a). In Europe, LSTIDs (Fig. 9c) that were launched
279 by dayside ionospheric currents over Svalbard were observed propagating equatorward to mid
280 latitudes between 11:00 and 18:00 UT (Fig. 10b).

281

282 In summary, the cases discussed in Sections 3.1 and 3.2 highlight the importance of solar wind
283 coupling to the M-I-T system, particularly on the dayside, in the generation of AGWs/TIDs. The



284 fluctuations of the IMF, sometimes Alfvénic, modulate the ionospheric currents in the cusp driving
285 TIDs. Intensifications of auroral electrojets launch LSTIDs.

286

287 **4. AGWs/TIDs originating from sources in the troposphere**

288

289 In this section we focus on MSTIDs in mid latitudes that originated from tropospheric weather
290 systems and were observed by HF Doppler sounders as well as by the GNSS TEC mapping
291 technique. The animations of detrended TEC maps (see Video in the Supplement) display TIDs
292 motions with varying azimuths. At high latitudes, they propagate predominantly equatorward
293 suggesting likely auroral sources. At mid to low latitudes, the azimuth of MSTIDs varies,
294 suggesting sources in the troposphere.

295

296 MSTIDs caused by GWs with periods of 10-40 min propagating obliquely upward in the
297 thermosphere/ionosphere were studied using multi-frequency and multi-point continuous HF
298 Doppler sounding system located in the western part of Czechia from July 2014 to June 2015
299 (Chum et al., 2021). The observed azimuths depend on season with southeastward propagation
300 more likely in winter months, suggesting that cold season low pressure systems in the northeast
301 Atlantic are sources of the GWs, which supports previously published results referenced above
302 and points to winter jet stream as a likely source of GWs. In this section we examine such cases
303 and trace TIDs in detrended TEC maps propagating from sources over the east Atlantic
304 eastward/southeastward, and over the HF Doppler sounders that observed the medium-scale GWs.

305

306 *4.1. Events of November 1-8, 2014*

307 The 2-D propagation analysis of the HF Doppler sounders data for several events was applied to
308 selected time intervals that exclude data gaps and to select time intervals in which the phase
309 shifts/time delays between signals corresponding to different sounding paths (transmitter-receiver
310 pairs) were approximately constant. Spectral and propagation analysis for all available 7.04 MHz
311 signals from November 1 to 8, 2014 was performed (Fig. 11). Only daytime values are available
312 because the critical frequency foF2 is too low at night (most of the nights are also not available at
313 4.65 MHz). On November 6 an enhanced noise (electromagnetic interference) prevented reliable
314 analysis for a substantial part of the day. Fig. 11b shows dynamic spectra (periodograms) of



315 Doppler shift signal obtained as the average of the maxima of three power spectral densities
316 corresponding to three different transmitter – receiver pairs (Section 2) shown in Fig. 11a
317 (including artificial offsets). The observed periods (Fig. 11b) range from 10 to about 40 min. The
318 propagation azimuths (Fig. 11c) were mostly from 100 to about 160° (waves propagating south-
319 eastward). In all cases, the azimuth is only plotted if the averaged Doppler fluctuations exceeded
320 0.12 Hz, the estimate of uncertainty of azimuth is less than 10° and the estimate of uncertainty in
321 velocity is less than 10%. The phase velocities fluctuated typically between 100 and 200 m/s. Fig.
322 12 shows the analysis results on an expanded time scale to better see the TID characteristics for
323 November 8.

324

325 During the period from November 1 to 8, 2014, we distinguish between aurorally-generated TIDs
326 propagating equatorward from high latitudes (Section 3.2) and south-eastward propagating
327 MSTIDs at mid latitudes by observed origin location. The south-eastward propagating MSTIDs
328 were observed by the HF sounders and detrended vTEC. Low-pressure systems deepening over
329 the North-east Atlantic, shown in the surface pressure analysis charts
330 (https://www1.wetter3.de/archiv_ukmet_dt.html), were likely sources of MSTIDs propagating
331 eastward to southeastward, as observed in the detrended vTEC maps (indicated by arrows in Figs.
332 13a,b) on November 1 and 8, 2014. At the same time, the vTEC maps on both days also reveal
333 equatorward propagating TIDs at latitudes down to ~50°N that originated in the cusp ionospheric
334 footprint over Svalbard, as already discussed in Section 3.2.

335

336 The Doppler shift spectrograms (Fig. 14a) recorded at frequency 7.04 MHz on November 1 and 8,
337 2014 show temporal evolution of power spectral densities (color-coded arbitrary units) of received
338 signals that correspond to three different transmitter-receiver pairs. There was enhanced noise due
339 to the electromagnetic interference on 8 November from about 9:30 to 12:30 UT. The straight
340 horizontal line in the upper signal trace in the spectrogram corresponds to ground wave from one
341 of the transmitters, located only ~7 km from the receiver. The middle and bottom signal traces in
342 the spectrogram correspond to other two transmitters. As described in more detail by Chum and
343 Podolská (2018) and Chum et al. (2021), the use of well correlated signals at two or three different
344 frequencies makes it possible to determine a 3-D phase velocity vector. The results that are
345 summarized in Table S1 in the Supplement separately for the observation at frequencies of 4.65



346 and 7.04 MHz show mostly similar values of horizontal velocities (ranging from ~100 to 200 m/s)
347 and azimuths (ranging from ~90 to 145°).

348

349 In Fig. 14b (middle panels), the detrended vTEC mapped along the latitude of 50° shows eastward
350 propagating TIDs towards the longitude of the HF sounding system that observed the TIDs (top
351 panels). The bottom panels (Fig. 14c) show time series of the detrended vTEC at longitude of 7°E
352 and the normalized FFT spectra that show peaks at periodicities of MSTIDs similar to those in
353 Figs. 11b and 12b.

354

355 Cases of MSTIDs associated with intense low pressure systems were also observed on November
356 3 (~08:00-13:00 UT) (see Fig. S5 in the Supplement), November 7 (~08:00-13:00 UT) (see Fig.
357 S6 in the Supplement), November 22 (~08:00-09:00 UT), November 24 (~07:30-10:30 UT),
358 December 9 (~08:30-09:50 and 12:00-13:50 UT), December 10 (~07:30-09:50 and 12:00-13:30
359 UT), and December 24 (~10:00-14:00 UT).

360

361 In summary, the south-eastward propagating MSTIDs observed in the detrended vTEC maps and
362 by the HF Doppler sounders likely originated from intense low-pressure systems in the North-east
363 Atlantic.

364

365 *4.2. Physical mechanism of GW generation in the troposphere*

366 While tropospheric convection is a common source of gravity waves, no deep convection could be
367 identified in the cold fronts of low-pressure systems over the North-east Atlantic
368 (<https://www.ncdc.noaa.gov/gibbs/html/MSG-3/IR/2014-11-01-0>). Mesoscale gravity waves
369 generated by geostrophic adjustment processes and shear instability have been observed (Uccellini
370 and Koch, 1987; Koch and Dorian, 1988). Plougonven and Zhang (2014) reviewed the current
371 knowledge and understanding of gravity waves near jets and fronts. Plougonven and Teitelbaum
372 (2003; their Figure 2) showed patterns of alternating bands of convergence and divergence in maps
373 of divergence of the horizontal wind for the lower stratosphere, which have been interpreted as the
374 signature of inertia-gravity waves propagating upwards above the tropopause. A conceptual model
375 of a common synoptic pattern has been identified with a source of gravity waves near the axis of
376 inflection in the 300-hPa geopotential height field (Koch and O'Handley, 1997; their Figure 2).



377

378 In Section 4.1, the cases of MSTIDs on November 1 and 8, 2014 (Figs. 13 and 14) propagating
379 eastward to southeastward observed by the HF Doppler sounding system and in the detrended
380 vTEC maps are attributed to sources in the troposphere, namely deepening low pressure weather
381 systems. This is consistent with the conceptual model referenced above. Using the ERA5
382 reanalysis (Hersbach *et al.*, 2020), Fig. 15 shows the 300-hPa geopotential height, approximate
383 axis of inflection (a probable source region of gravity waves that is indicated by red dashed line),
384 and horizontal winds at 300 hPa on November 1 and 8, 2014. Fig. 15b shows the divergence of
385 the horizontal wind at 150-hPa level. The alternating bands of convergence and divergence are
386 similar to those interpreted by Plougonven and Teitelbaum (2003) as gravity waves propagating
387 to the lower stratosphere. Other cases of MSTIDs on November 3 and 7 can be viewed in Figs. S5
388 and S6 in the Supplement.

389

390 As mentioned in Section 3, in the case of the TID event over Alaska on January 8/9, 2013 that we
391 attributed to auroral sources poleward of Alaska, Bossert *et al.* (2021) observed GWs generated
392 by stratospheric vortex. There was an extratropical cyclone intensifying just south-west of Alaska.
393 Using the ERA5 reanalysis, similar to Figs. 15e,f, north-eastward propagating GWs in the
394 stratosphere are found (Fig. S7 in the Supplement) but no corresponding TIDs can be resolved in
395 the detrended TEC maps, possibly because of sparse coverage by GNSS receivers. However,
396 mesoscale GWs propagating eastward and upward into the stratosphere generated by geostrophic
397 adjustment processes and shear instability may be common and could be driving MSTIDs.

398

399 **5. Discussion**

400 The solar wind – MIT coupling is known to modulate the intensity of ionospheric currents,
401 including the auroral electrojets, which in turn launch atmospheric gravity waves causing TIDs.
402 The cases of dayside equatorward propagating TIDs were observed with PFISR, SuperDARN, and
403 detected in the detrended GNSS vTEC maps. This is consistent with previously published results
404 and interpretations (e.g., Prikryl *et al.* 2022; and references therein). The dayside TIDs are
405 commonly generated in the ionospheric footprint of the cusp. They were observed every day over
406 Alaska during the PFISR experiment (8-15 January 2013) and in Europe (1-8 November 2014).

407



408 In Section 3.1, we have shown evidence that even during a geomagnetically very quiet period the
409 TIDs that were observed by PFISR in Alaska can be attributed to sources at high latitudes.
410 Quasiperiodic intensifications of the high-latitude ionospheric convection that were the source of
411 these TIDs were observed poleward of Alaska over the East Siberian and Beaufort Seas. The
412 ionospheric currents associated with PIFs could not be detected by ground magnetometers, and the
413 Kp index indicated a quiet period. The ionospheric footprint of the cusp where the pulsed
414 ionospheric flows and associated currents are sources of TIDs may be located further poleward of
415 any ground magnetometers.

416

417 Regarding TIDs originating from the troposphere, there has been plentiful evidence of neutral
418 atmosphere-ionosphere coupling via atmospheric gravity waves propagating into the upper
419 atmosphere from sources in the lower atmosphere including convective storms (Alexander, 1996).
420 Azeem and Barlage (2018) and Vadas and Azeem (2021) presented cases of convective storm
421 generating TIDs, which exhibited partial to full concentric, or almost plane-parallel phase fronts.
422 The latter TIDs were generated by extended squall line (Azeem and Barlage, 2018). However, in
423 the cases discussed in Section 4.1 there was no significant convection in the cold fronts that would
424 generate such TIDs. The eastward propagating MSTIDs observed in the detrended $vTEC$ maps
425 and by the HF originated from low pressure sounding system were likely driven by GWs generated
426 by geostrophic adjustment processes and shear instability in the troposphere.

427

428 In this study we have attempted to trace the observed TIDs to sources of AGWs in the upper and
429 lower atmosphere, and to identify physical mechanisms. The solar wind coupling to the M-I-T
430 system can generate equatorward propagating TIDs even during geomagnetically quiet conditions.
431 Intensifying low pressure weather systems can generate AGWs propagating to the lower
432 stratosphere and beyond, driving TIDs even when there is no significant tropospheric convection.
433 More work needs to be done to better understand such cases, and many aspects of the system as a
434 whole should be considered when determining the source of TIDs, as simple metrics/indices hide
435 critical details.

436

437 **6. Summary and conclusions**



438 Traveling ionospheric disturbances are observed by radars, Doppler sounders, and the GNSS TEC
439 mapping technique. Medium- to large-scale TIDs propagating equatorward were generated by
440 solar wind coupling to the dayside magnetosphere-ionosphere-thermosphere modulating
441 ionospheric convection and currents, including auroral electrojets. TIDs that were observed over
442 Alaska by the Poker Flat incoherent scatter radar and by two SuperDARN radars are attributed to
443 gravity waves generated in the ionospheric cusp footprint poleward of Alaska even when
444 geomagnetic activity was low. Major intensifications of the westward electrojet over the North
445 American sector launched LSTIDs observed by a mid-latitude SuperDARN radar and in the
446 detrended global TEC maps. In the European sector, the equatorward propagating TIDs are
447 attributed to solar wind Alfvén waves coupling to the dayside magnetosphere modulating
448 ionospheric convection and currents in the cusp footprint over Svalbard. The cases of eastward to
449 southeastward propagating MSTIDs observed at mid latitudes in the detrended GNSS TEC maps
450 and by the HF Doppler sounders in Czechia originated from low pressure systems. The likely cause
451 of these TIDs were gravity waves propagating from the troposphere and lower stratosphere that
452 were generated by geostrophic adjustment processes, which have rarely been linked to TIDs
453 previously.

454

455 *Data availability.* The solar wind data are provided by the NSSDC OMNI
456 (<http://omniweb.gsfc.nasa.gov>; NASA, 2022). The ground-based magnetometer data are
457 archived at the website of the Canadian Array for Realtime Investigations of Magnetic Activity
458 (CARISMA) (<https://www.carisma.ca/>; University of Alberta, 2022), and the IMAGE website at
459 <https://space.fmi.fi/image/www/index.php?>. The PFISR data are available
460 at <https://data.amisr.com/database/61/cal/2014/11/>. SuperDARN data are available
461 at <https://www.frdr-dfdr.ca/repo/collection/superdarn> (FRDR, 2022). Line-of-Sight TEC data can
462 be acquired from the Madrigal database (<http://cedar.openmadrigal.org/>; CEDAR, 2022) and
463 CHAIN GNSS data are available at http://chain.physics.unb.ca/chain/pages/data_download
464 (CHAIN, 2022).

465 Equivalent Ionospheric Currents (EICs) derived by the Spherical Elementary Currents Systems
466 (SECS) technique are archived at <http://vmo.igpp.ucla.edu/data1/SECS/> (SECS, 2022)
467 and [https://cdaweb.gsfc.nasa.gov/pub/data/aaa_special-purpose-datasets/spherical-elementary-
468 and-equivalent-ionospheric-currents-weygand/](https://cdaweb.gsfc.nasa.gov/pub/data/aaa_special-purpose-datasets/spherical-elementary-and-equivalent-ionospheric-currents-weygand/); <https://doi.org/10.21978/P8D62B>, Weygand,



469 2009a; <https://doi.org/10.21978/P8PPP8X>, Weygand, 2009b). The Czech HF Doppler shift
470 spectrograms can be found in the archive at <http://datacenter.ufa.cas.cz/>.

471 GNSS data for this study were provided by the following organizations: International GNSS
472 Service (IGS), UNAVCO (<https://www.unavco.org/data/gps-gnss/gps-gnss.html>), Dutch
473 Permanent GNSS Array (<http://gnss1.tudelft.nl/dpga/rinex>), Can-Net (<https://www.can-net.ca/>),
474 Scripps Orbit and Permanent Array Center (Garner, <http://garner.ucsd.edu/pub/>), French Institut
475 Geographique National, Geodetic Data Archiving Facility (GeoDAF,
476 <http://geodaf.mt.asi.it/index.html>), Crustal Dynamics Data Information System (CDDIS,
477 <https://cddis.nasa.gov/archive/gnss/data/daily/>), National Geodetic Survey
478 (<https://geodesy.noaa.gov/corsdata/>), Instituto Brasileiro de Geografia e Estatistica
479 (http://geofp.ibge.gov.br/informacoes_sobre_posicionamento_geodesico/rbmc/dados/), Instituto
480 Tecnológico Agrario de Castilla y Leon (ITACyL, <ftp://ftp.itacyl.es/RINEX/>), TrigNet South
481 Africa (<ftp://ftp.trignet.co.za>), The Western Canada Deformation Array (WCDA,
482 <ftp://wcda.pgc.nrcan.gc.ca/pub/gpsdata/rinex>), Canadian High Arctic Ionospheric Network
483 (CHAIN, http://chain.physics.unb.ca/chain/pages/data_download), Pacific Northwest Geodetic
484 Array (PANGA, <http://www.geodesy.cwu.edu/pub/data/>), Centro di Ricerche Sismologiche,
485 Système d'Observation du Niveau des Eaux Littorales (SONEL, <ftp://ftp.sonel.org/gps/data>),
486 INGV - Rete Integrata Nazionale GPS (RING, <http://ring.gm.ingv.it>), RENAG : REseau
487 NAtional GPS permanent (<http://rgp.ign.fr/DONNEES/diffusion/>), Australian Space Weather
488 Services (<https://downloads.sws.bom.gov.au/wdc/gnss/data/>), GeoNet New Zealand
489 (<https://www.geonet.org.nz/data/types/geodetic>), National Land Survey Finland (NLS,
490 <https://www.maanmittauslaitos.fi/en/maps-and-spatial-data/positioning-services/rinex-palvelu>),
491 SWEPOS Sweden (<https://swepos.lantmateriet.se/>), Norwegian Mapping Authority (Kartverket,
492 <https://ftp.statkart.no/>), Geoscience Australia ([http://www.ga.gov.au/scientific-
493 topics/positioning-navigation/geodesy/gnss-networks/data-and-site-logs](http://www.ga.gov.au/scientific-topics/positioning-navigation/geodesy/gnss-networks/data-and-site-logs)), Institute of
494 Geodynamics, National Observatory of Athens (<https://www.gein.noa.gr/services/GPSData/>), and
495 European Permanent GNSS Network (EUREF,
496 https://www.epncb.oma.be/networkdata/data_access/dailyandhourly/datacentres.php).

497 *Author contributions.* PP and RGG contributed to conception and design of the study. PP, DRT,
498 JC, SC, RGG, and JMW acquired the resources and contributed to methodology, software, specific



499 data analysis, visualization, and organized the databases. PP wrote the first draft of the manuscript.
500 All authors contributed to manuscript revision and approved the submitted version.
501 *Competing interests.* The authors declare that they have no conflict of interest.
502 *Acknowledgments.* Infrastructure funding for CHAIN was provided by the Canada Foundation for
503 Innovation and the New Brunswick Innovation Foundation. CHAIN operation is conducted in
504 collaboration with the Canadian Space Agency (CSA). We are grateful to the Australian Bureau
505 of Meteorology, Space Weather Services for the provision of GNSS data. CDDIS is one of the
506 Earth Observing System Data and Information System (EOSDIS) Distributed Active Archive
507 Centers (DAACs), part of the NASA Earth Science Data and Information System (ESDIS) project.
508 Datasets and related data products and services are provided by CDDIS, managed by the NASA
509 ESDIS project. This material is based on services provided by the GAGE Facility, operated by
510 UNAVCO, Inc., with support from the National Science Foundation and the National Aeronautics
511 and Space Administration under NSF Cooperative Agreement EAR-1724794. A. Contributions by
512 the ACE (Norman F. Nees at Bartol Research Institute, David J. McComas at SWRI), NASA's
513 SPDF/CDAWeb, and the NSSDC OMNIWeb are acknowledged. The PFISR was developed under
514 NSF cooperative agreement ATM-0121483, and the data collection and analysis were supported
515 under NSF cooperative agreement ATM-0608577. The authors acknowledge the use of
516 SuperDARN data. SuperDARN is a collection of radars funded by the national scientific funding
517 agencies of Australia, Canada, China, France, Italy, Japan, Norway, South Africa, United
518 Kingdom, and the United States of America. The Fort Hays SuperDARN radars are maintained
519 and operated by Virginia Tech under support by NSF grant AGS-1935110. We thank the many
520 different groups operating magnetometer arrays for providing data for this study, including the
521 THEMIS UCLA magnetometer network (Ground-based Imager and Magnetometer Network for
522 Auroral Studies). The AUTUMNX magnetometer network is funded through the Canadian Space
523 Agency/Geospace Observatory (GO) Canada program, Athabasca University, Centre for
524 Science/Faculty of Science and Technology. The Magnetometer Array for Cusp and Cleft Studies
525 (MACCS) array is supported by the US National Science Foundation grant ATM-0827903 to
526 Augsburg College. The Solar and Terrestrial Physics (STEP) magnetometer file storage is at the
527 Department of Earth and Planetary Physics, University of Tokyo and maintained by Kanji Hayashi
528 (hayashi@grl.s.u-tokyo.ac.jp). The McMAC Project is sponsored by the Magnetospheric Physics
529 Program of National Science Foundation through grant AGS-0245139. The ground magnetic



530 stations are operated by the Technical University of Denmark, National Space Institute (DTU
531 Space). The IMAGE magnetometer stations are maintained by 10 institutes from Finland,
532 Germany, Norway, Poland, Russia, Sweden, Denmark, and Iceland. The Canadian Space Science
533 Data Portal is funded in part by the Canadian Space Agency contract numbers 9 F007-071429 and
534 9 F007-070993. The Canadian Magnetic Observatory Network (CANMON) is maintained and
535 operated by the Geological Survey of Canada. David R. Themens's contribution to this work is
536 supported in part through CSA grant no. 21SUSTCHAI and through the United Kingdom Natural
537 Environment Research Council (NERC) EISCAT3D: Fine-scale structuring, scintillation, and
538 electrodynamics (FINESSE) (NE/W003147/1) and DRivers and Impacts of Ionospheric
539 Variability with EISCAT-3D (DRIIVE) (NE/W003368/1) projects. James M. Weygand
540 acknowledges NASA grant: 80NSSC18K0570, 80NSSC18K1220, NASA contract:
541 80GSFC17C0018 (HPDE), NAS5-02099(THEMIS). Shibaji Chakraborty thanks the National
542 Science Foundation for support under grant AGS-1935110.

543

544 *Financial support.* David R. Themens's contribution to this work is supported in part through CSA
545 grant no. 21SUSTCHAI and through the United Kingdom Natural Environment Research Council
546 (NERC) EISCAT3D: Fine-scale structuring, scintillation, and electrodynamics (FINESSE)
547 (NE/W003147/1) and DRivers and Impacts of Ionospheric Variability with EISCAT-3D
548 (DRIIVE) (NE/W003368/1) projects. J. Chum was funded by T-FORS project by European
549 Commission (number SEP 210818055) and by the Johannes Amos Comenius Programme (P JAC),
550 project No. CZ.02.01.01/00/22_008/0004605, Natural and anthropogenic georisks“. James M. Weygand is supported by the NASA grant: 80NSSC18K0570, 80NSSC18K1220,
551 NASA contract: 80GSFC17C0018 (HPDE), NAS5-02099(THEMIS). Shibaji Chakraborty is
552 supported by the National Science Foundation under grant AGS-1935110.
553

554

555 **References**

556

557 Alexander, M. J.: A simulated spectrum of convectively generated gravity waves: Propagation
558 from the tropopause to the mesopause and effects on the middle atmosphere, *Journal of*
559 *Geophysical Research: Atmospheres*, 101(D1), pp. 1571–1588. doi:
560 <https://doi.org/10.1029/95JD02046>, 1996.

561 Azeem, I. et al.: Multisensor profiling of a concentric gravity wave event propagating from the
562 troposphere to the ionosphere, *Geophysical Research Letters*, 42(19), pp. 7874–7880. doi:
563 <https://doi.org/10.1002/2015GL065903>, 2015.

564 Azeem, I. and Barlage, M.: Atmosphere-ionosphere coupling from convectively generated
565 gravity waves, *Advances in Space Research*, 61(7), pp. 1931–1941. doi:



- 566 <https://doi.org/10.1016/j.asr.2017.09.029>, 2018.
- 567 Azeem, I.: Asymmetry of near-noncentric traveling ionospheric disturbances due to Doppler-
568 shifted atmospheric gravity waves, *Frontiers in Astronomy and Space Sciences*, 8,
569 <https://doi.org/10.3389/fspas.2021.690480>, 2021.
- 570 Balthazor, R. L. and J., R.: A study of atmospheric gravity waves and travelling ionospheric
571 disturbances at equatorial latitudes, *Ann. Geophys.*, 15. Available at: [http://www.ann-](http://www.ann-geophys.net/15/1048/1997/)
572 [geophys.net/15/1048/1997/](http://www.ann-geophys.net/15/1048/1997/), 1997.
- 573 Becker, E., Vadas, S. L., Goncharenko, L., and Harvey, V. L.: Multi-step vertical coupling from
574 the troposphere to the thermosphere due to gravity waves, in *EGU General Assembly*
575 *Conference Abstracts*, pp. EGU22-10900. doi: 10.5194/egusphere-egu22-10900, 2022.
- 576 Belcher, J. W., and Davis, L., Jr.: Large-amplitude Alfvén waves in the interplanetary medium,
577 *J. Geophys. Res.*, 76, 3534–3563, 1971.
- 578 Bertin, F., Testud, J., Kersley, L., and Rees, P. R.: The meteorological jet stream as a source of
579 medium scale gravity waves in the thermosphere: an experimental study, *Journal of Atmospheric*
580 *and Terrestrial Physics*, 40(10), pp. 1161–1183. doi: [https://doi.org/10.1016/0021-](https://doi.org/10.1016/0021-9169(78)90067-3)
581 [9169\(78\)90067-3](https://doi.org/10.1016/0021-9169(78)90067-3), 1978.
- 582 Bertin, F., Testud, J. and Kersley, L.: Medium scale gravity waves in the ionospheric F-region
583 and their possible origin in weather disturbances, *Planetary and Space Science*, 23(3), pp. 493–
584 507. doi: [https://doi.org/10.1016/0032-0633\(75\)90120-8](https://doi.org/10.1016/0032-0633(75)90120-8), 1975.
- 585 Bossert, K., Becker, E., Kumari, K., and Conde, M.: Observations of stratospheric vortex
586 generated gravity waves and subsequent impacts on thermosphere/ionosphere variability and
587 traveling ionospheric disturbance generation, in *AGU Fall Meeting Abstracts*, pp. SA11B-07,
588 2021.
- 589 Bristow, W. A., Greenwald, R. A. and Samson, J. C.: Identification of high-latitude acoustic
590 gravity wave sources using the Goose Bay HF Radar, *Journal of Geophysical Research: Space*
591 *Physics*, 99(A1), pp. 319–331. doi: <https://doi.org/10.1029/93JA01470>, 1994.
- 592 Cai, H. T., Yin, F., Ma, S. Y., and McCrea, I. W.: Observations of AGW/TID propagation across
593 the polar cap: a case study, *Annales Geophysicae*, 29(8), pp. 1355–1363. doi: 10.5194/angeo-29-
594 1355-2011, 2011.
- 595 Chimonas, G.: The equatorial electrojet as a source of long period travelling ionospheric
596 disturbances, *Planetary and Space Science*, 18(4), pp. 583–589. doi:
597 [https://doi.org/10.1016/0032-0633\(70\)90133-9](https://doi.org/10.1016/0032-0633(70)90133-9), 1970.
- 598 Chimonas, G. and Hines, C. O.: Atmospheric gravity waves launched by auroral currents,
599 *Planetary and Space Science*, 18(4), pp. 565–582. doi: 10.1016/0032-0633(70)90132-7, \1970.
- 600 Chum J., Podolská K.: 3D analysis of GW propagation in the ionosphere. *Geophysical Research*
601 *Letters*, 45, 11,562–11,571, <https://doi.org/10.1029/2018GL079695>, 2018.



- 602
- 603 Chum, J., Podolská, K., Rusz, J., Baše, J., and Tedoradze, N.: Statistical investigation of gravity
604 wave characteristics in the ionosphere, *Earth, Planets and Space*, 73(1), p. 60. doi:
605 10.1186/s40623-021-01379-3, 2021.
- 606 Crowley, G. and Williams, P. J. S.: Observations of the source and propagation of atmospheric
607 gravity waves, *Nature*, 328(6127), pp. 231–233. doi: 10.1038/328231a0, 1988.
- 608 Dungey, J. W.: Interplanetary Magnetic Field and the Auroral Zones. *Phys. Rev. Lett.* 6, 47–48.
609 <https://doi.org/10.1103/PhysRevLett.6.47>, 1961.
- 610 Dungey, J. W.: Origin of the concept of reconnection and its application to the magnetopause: A
611 historical view, *Physics of the Magnetopause. Geophysical Monograph 90*, edited by P. Song,
612 B.U.O. Sonnerup, and M.F. Thomsen, pp. 17–19, AGU, Washington, D.C., 1995.
- 613 Frissell, N. A., Baker, J. B. H., Ruohoniemi, J. M., Gerrard, A. J., Miller, E. S., Marini, J. P.,
614 West, M. L., and Bristow, W. A.: Climatology of medium-scale traveling ionospheric
615 disturbances observed by the midlatitude Blackstone SuperDARN radar, *Journal of Geophysical*
616 *Research: Space Physics*, 119(9), pp. 7679–7697. doi: <https://doi.org/10.1002/2014JA019870>,
617 2014.
- 618 Frissell, N. A., Baker, J. B. H., Ruohoniemi, J. M., Greenwald, R. A., Gerrard, A. J., Miller, E.
619 S., and West, M. L.: Sources and characteristics of medium-scale traveling ionospheric
620 disturbances observed by high-frequency radars in the North American sector, *Journal of*
621 *Geophysical Research: Space Physics*, 121(4), pp. 3722–3739,
622 <https://doi.org/10.1002/2015JA022168>, 2016.
- 623 Goncharenko, L., Harvey, V. L., Cullens, C., Becker, E., Zhang, S.-R., and Coster, A.: Influence
624 of stratospheric gravity waves on TID activity at middle latitudes, in *EGU General Assembly*
625 *Conference Abstracts*, pp. EGU22-6823, doi: 10.5194/egusphere-egu22-6823, 2022.
- 626 Gonzalez, W. D., Joselyn, J. A., Kamide, Y., Kroehl, H. W., Rostoker, G., Tsurutani, B. T., and
627 Vasyliunas, V. M.: What is a geomagnetic storm?, *Journal of Geophysical Research: Space*
628 *Physics*, 99(A4), pp. 5771–5792, doi: <https://doi.org/10.1029/93JA02867>, 1994.
- 629 Hajkowicz, L. A.: Auroral electrojet effect on the global occurrence pattern of large scale
630 travelling ionospheric disturbances, *Planetary and Space Science*, 39(8), pp. 1189–1196., doi:
631 [https://doi.org/10.1016/0032-0633\(91\)90170-F](https://doi.org/10.1016/0032-0633(91)90170-F), 1991.
- 632 Heinselman, C. J. and Nicolls, M. J.: A Bayesian approach to electric field and E-region neutral
633 wind estimation with the Poker Flat Advanced Modular Incoherent Scatter Radar, *Radio Science*,
634 43(5). doi: <https://doi.org/10.1029/2007RS003805>, 2008.
- 635 Hersbach, H., Bell, B., Berrisford, P., Hirahara, S., Horányi, A., Muñoz-Sabater, J., Nicolas, J.,
636 Peubey, C., Radu, R., Schepers, D., Simmons, A., Soci, C., Abdalla, S., Abellan, X., Balsamo,
637 G., Bechtold, P., Biavati, G., Bidlot, J., Bonavita, M., De Chiara, G., Dahlgren, P., Dee, D.,
638 Diamantakis, M., Dragani, R., Flemming, J., Forbes, R., Fuentes, M., Geer, A., Haimberger, L.,



- 639 Healy, S., Hogan, R. J., Hólm, E., Janisková, M., Keeley, S., Laloyaux, P., Lopez, P., Lupu, C.,
640 Radnoti, G., de Rosnay, P., Rozum, I., Vamborg, F., Villaume, S., and Thépaut, J.-N.: The ERA5
641 global reanalysis, *Q. J. R. Met. Soc.*, 146(730), pp. 1999–2049. doi:
642 <https://doi.org/10.1002/qj.3803>, 2020.
- 643 Hines, C. O.: Internal Atmospheric Gravity Waves At Ionospheric Heights, *Canadian Journal of*
644 *Physics*, 38(11), pp. 1441–1481. doi: 10.1139/p60-150, 1960.
- 645 Hocke, K. and Schlegel, K.: A review of atmospheric gravity waves and travelling ionospheric
646 disturbances: 1982-1995, *Annales Geophysicae*, 14(9), pp. 917–940, doi: 10.1007/s00585-996-
647 0917-6, 1996.
- 648 Huang, C.-S., Sofko, G. J., Kustov, A. V, MacDougall, J. W., Andre, D. A., Hughes, W. J., and
649 Papitashvili, V. O.: Quasi-periodic ionospheric disturbances with a 40-min period during
650 prolonged northward interplanetary magnetic field, *Geophysical Research Letters*, 27(12), pp.
651 1795–1798, doi: <https://doi.org/10.1029/1999GL003731>, 2000.
- 652 Huang, C.-S., Andre, D. A. and Sofko, G. J.: Observations of solar wind directly driven auroral
653 electrojets and gravity waves, *Journal of Geophysical Research: Space Physics*, 103(A10), pp.
654 23347–23356. doi: <https://doi.org/10.1029/98JA02297>, 1998.
- 655 Hunsucker, R. D.: Atmospheric gravity waves generated in the high-latitude ionosphere: A
656 review, *Reviews of Geophysics*, 20(2), pp. 293–315, doi: 10.1029/RG020i002p00293, 1982.
- 657 van de Kamp, M., Pokhotelov, D. and Kauristie, K.: TID characterised using joint effort of
658 incoherent scatter radar and GPS, *Annales Geophysicae*, 32(12), pp. 1511–1532, doi:
659 10.5194/angeo-32-1511-2014, 2014.
- 660 Kelley, I. J., Kunduri, B. S. R., Baker, J. B. H., Ruohoniemi, J. M., and Shepherd, S. G.: Storm
661 Time Electrified MSTIDs Observed Over Mid-Latitude North America, *Journal of Geophysical*
662 *Research: Space Physics*, 128(3), p. e2022JA031115, doi:
663 <https://doi.org/10.1029/2022JA031115>, 2023.
- 664 Kikuchi, T., Hashimoto, K.K.: Transmission of the electric fields to the low latitude ionosphere
665 in the magnetosphere-ionosphere current circuit, *Geosci. Lett.* 3, 4,
666 <https://doi.org/10.1186/s40562-016-0035-6>, 2014.
- 667 King, J. H. and Papitashvili, N.: Solar wind spatial scales in and comparisons of hourly Wind
668 and ACE plasma and magnetic field data, *Journal of Geophysical Research*, 110(A2), p. A02104.
669 doi: 10.1029/2004JA010649, 2005.
- 670 Klostermeyer, J.: Lamb waves originating in nongeostrophic disturbances: A case study, *J.*
671 *Geophys. Res.*, 82(9), 1441–1448, doi: [10.1029/JC082i009p01441](https://doi.org/10.1029/JC082i009p01441), 1977.
- 672 Koch, S. E. and Dorian, P. B.: A Mesoscale Gravity Wave Event Observed during CCOPE. Part
673 III: Wave Environment and Probable Source Mechanisms, *Monthly Weather Review*, 116(12),
674 pp. 2570–2592. doi: [https://doi.org/10.1175/1520-0493\(1988\)116<2570:AMGWEO>2.0.CO;2](https://doi.org/10.1175/1520-0493(1988)116<2570:AMGWEO>2.0.CO;2),
675 1988.



- 676 Koch, S. E. and OHandley, C.: Operational Forecasting and Detection of Mesoscale Gravity
677 Waves, *Weather and Forecasting*, 12(2), pp. 253–281, doi: [https://doi.org/10.1175/1520-0434\(1997\)012<0253:OFADOM>2.0.CO;2](https://doi.org/10.1175/1520-0434(1997)012<0253:OFADOM>2.0.CO;2), 1997.
- 679 Lewis, R. V., Williams, P. J. S., Millward, G. H., and Quegan, S.: The generation and
680 propagation of atmospheric gravity waves from activity in the auroral electrojet, *Journal of*
681 *Atmospheric and Terrestrial Physics*, 58(6), pp. 807–820, doi: [https://doi.org/10.1016/0021-9169\(95\)00075-5](https://doi.org/10.1016/0021-9169(95)00075-5), 1996.
- 683 Mayr, H. G., Harris, I., Varosi, F., and Herrero, F. A.: Global Excitation of Wave Phenomena in
684 a Dissipative Multiconstituent Medium. 1. Transfer Function of the EarthS Thermosphere,
685 *Journal of Geophysical Research*, 89(A12), pp. 10929–10959, doi: [10.1029/JA089iA12p10929](https://doi.org/10.1029/JA089iA12p10929),
686 1984a.
- 687 Mayr, H. G., Harris, I., Varosi, F., and Herrero, F. A.: Global Excitation of Wave Phenomena in
688 a Dissipative Multiconstituent Medium - 2. Impulsive Perturbations in the EarthS Thermosphere,
689 *Journal of Geophysical Research*, 89(A12), pp. 10961–10986. doi: [10.1029/JA089iA12p10961](https://doi.org/10.1029/JA089iA12p10961),
690 1984b.
- 691 Mayr, H. G., Talaat, E. R. and Wolven, B. C.: Global propagation of gravity waves generated
692 with the whole atmosphere transfer function model, *Journal of Atmospheric and Solar-Terrestrial*
693 *Physics*, 104, pp. 7–17, doi: [10.1016/j.jastp.2013.08.001](https://doi.org/10.1016/j.jastp.2013.08.001), 2013.
- 694 McWilliams, K. A., Yeoman, T. K. and Provan, G.: A statistical survey of dayside pulsed
695 ionospheric flows as seen by the CUTLASS Finland HF radar, *Annales Geophysicae*, 18(4), pp.
696 445–453, doi: [10.1007/s00585-000-0445-8](https://doi.org/10.1007/s00585-000-0445-8), 2000.
- 697 Milan, S. E., Gosling, J. S., and Hubert, B.: Relationship between interplanetary parameters and
698 the magnetopause reconnection rate quantified from observations of the expanding polar cap, *J.*
699 *Geophys. Res.*, 117, A03226, doi:[10.1029/2011JA017082](https://doi.org/10.1029/2011JA017082) 2012.
- 700 Millward, G.: A resonance effect in AGWs created by periodic recurrent bursts in the auroral
701 electric field, *Annales Geophysicae*, 12(1), pp. 94–94, 1994.
- 702 Millward, G. H., Quegan, S., Moffett, R. J., Fuller-Rowell, T. J., and Rees, D.: A modelling
703 study of the coupled ionospheric and thermospheric response to an enhanced high-latitude
704 electric field event, *Planetary and Space Science*, 41(1), pp. 45–56, doi: [10.1016/0032-0633\(93\)90016-U](https://doi.org/10.1016/0032-0633(93)90016-U), 1993a.
- 706 Millward, G. H., Moffett, R. J., Quegan, S., and Fuller-Rowell, T. J.: Effects of an atmospheric
707 gravity wave on the midlatitude ionospheric F layer, *Journal of Geophysical Research: Space*
708 *Physics*, 98(A11), pp. 19173–19179. doi: [10.1029/93ja02093](https://doi.org/10.1029/93ja02093), 1993b.
- 709 Mrak, S., Semeter, J., Nishimura, Y., Hirsch, M., and Sivadas, N.: Coincidental TID Production
710 by Tropospheric Weather During the August 2017 Total Solar Eclipse, *Geophysical Research*
711 *Letters*, 45(20), pp. 10,903-910,911, doi: <https://doi.org/10.1029/2018GL080239>, 2018.
- 712 Munteanu, C., Hamada, A., and Mursula, K.: High-speed solar wind streams in 2007-2008:



- 713 Turning on the Russell-McPherron effect, *Journal of Geophysical Research: Space Physics*, 124,
714 <https://doi.org/10.1029/2019JA026846>, 2019.
- 715 Negrea, C., Munteanu, C., and Echim, M. M.: Global ionospheric response to a periodic
716 sequence of HSS/CIR events during the 2007–2008 solar minimum, *Journal of Geophysical*
717 *Research: Space Physics*, 126, e2020JA029071, <https://doi.org/10.1029/2020JA029071>, 2021.
- 718 Nicolls, M. J., and Heinselman, C. J.: Three-dimensional measurements of traveling
719 ionospheric disturbances with the Poker Flat Incoherent Scatter Radar, *Geophys. Res. Lett.*, 34,
720 L21104, doi:[10.1029/2007GL031506](https://doi.org/10.1029/2007GL031506), 2007.
- 721 Nishioka, M., Tsugawa, T., Kubota, M., and Ishii, M.: Concentric waves and short-period
722 oscillations observed in the ionosphere after the 2013 Moore EF5 tornado, *Geophysical Research*
723 *Letters*, 40(21), pp. 5581–5586, doi: <https://doi.org/10.1002/2013GL057963>, 2013.
- 724 Nishitani, N., Ruohoniemi, J. M., Lester, M., Baker, J. B. H., Koustov, A. V., Shepherd, S. G.,
725 Chisham, G., Hori, T., Thomas, E. G., Makarevich, R. A., Marchaudon, A., Ponomarenko, P.,
726 Wild, J. A., Milan, S. E., Bristow, W. A., Devlin, J., Miller, E., Greenwald, R. A., Ogawa, T.,
727 and Kikuchi, T.: Review of the accomplishments of mid-latitude Super Dual Auroral Radar
728 Network (SuperDARN) HF radars, *Progress in Earth and Planetary Science*, 6(1), p. 27, doi:
729 10.1186/s40645-019-0270-5, 2019.
- 730 Oliver, W. L., Otsuka, Y., Sato, M., Takami, T., and Fukao, S.: A climatology of F region
731 gravity wave propagation over the middle and upper atmosphere radar, *Journal of Geophysical*
732 *Research: Space Physics*, 102(A7), pp. 14499–14512. doi: <https://doi.org/10.1029/97JA00491>,
733 1997.
- 734 Plougonven, R. and Teitelbaum, H.: Comparison of a large-scale inertia-gravity wave as seen in
735 the ECMWF analyses and from radiosondes, *Geophysical Research Letters*, 30(18), doi:
736 <https://doi.org/10.1029/2003GL017716>, 2003.
- 737 Plougonven, R. and Zhang, F.: Internal gravity waves from atmospheric jets and fronts, *Reviews*
738 *of Geophysics*, 52(1), pp. 33–76. doi: <https://doi.org/10.1002/2012RG000419>, 2014.
- 739 Press, W. H. and Teukolsky, S. A.: Savitzky-Golay Smoothing Filters, *Comput. Phys.* 4 (6):
740 669–672. <https://doi.org/10.1063/1.4822961>, 1990.
- 741 Prikryl, P., MacDougall, J. W., Grant, I. F., Steele, D. P., Sofko, G. J., and Greenwald, R. A.:
742 Polar patches generated by solar wind Alfvén wave coupling to the dayside magnetosphere,
743 *Advances in Space Research*, 23(10). doi: 10.1016/S0273-1177(99)00390-7, 1999.
- 744 Prikryl, P., Provan, G., McWilliams, K. A., and Yeoman, T. K.: Ionospheric cusp flows pulsed
745 by solar wind Alfvén waves, *Annales Geophysicae*, 20(2), doi: 10.5194/angeo-20-161-2002,
746 2002.
- 747 Prikryl, P., Muldrew, D. B., Sofko, G. J., and Ruohoniemi, J. M.: Solar wind Alfvén waves: A
748 source of pulsed ionospheric convection and atmospheric gravity waves, *Annales Geophysicae*,
749 23(2), pp. 401–417, doi: 10.5194/angeo-23-401-2005, 2005.



- 750 Prikryl, P., Gillies, R. G., Themens, D. R., Weygand, J. M., Thomas, E. G., and Chakraborty, S.:
751 Multi-instrument observations of polar cap patches and traveling ionospheric disturbances
752 generated by solar wind Alfvén waves coupling to the dayside magnetosphere, *Annales*
753 *Geophysicae*, 40(6), pp. 619–639, doi: 10.5194/angeo-40-619-2022, 2022.
- 754 Richmond, A. D.: Gravity wave generation, propagation, and dissipation in the thermosphere,
755 *Journal of Geophysical Research*, 83(A9), p. 4131, doi: 10.1029/ja083ia09p04131, 1978.
- 756 Samson, J. C., Greenwald, R. A., Ruohoniemi, J. M., Frey, A., Baker, K. B.: Goose bay radar
757 observations of earth-reflected, atmospheric gravity-waves in the high-latitude ionosphere, *J.*
758 *Geophys. Res.* 95(A6):7693–7709, <https://doi.org/10.1029/JA095iA06p07693>, 1990.
- 759 Smith, C. W., LHeureux, J., Ness, N. F., Acuña, M. H., Burlaga, L. F., and Scheifele, J.: The
760 ACE Magnetic Fields Experiment, *Space Science Reviews*, 86(1), pp. 613–632. doi:
761 10.1023/A:1005092216668, 1998.
- 762 Testud, J.: Gravity waves generated during magnetic substorms, *Journal of Atmospheric and*
763 *Terrestrial Physics*, 32(11), pp. 1793–1805, doi: 10.1016/0021-9169(70)90137-6, 1970.
- 764 Themens, D. R., Jayachandran, P. T., Langley, R. B., MacDougall, J. W., and Nicolls, M. J.:
765 Determining receiver biases in GPS-derived total electron content in the auroral oval and polar
766 cap region using ionosonde measurements, *GPS Solutions*, 17(3), pp. 357–369. doi:
767 10.1007/s10291-012-0284-6, 2013.
- 768 Themens, D. R., Watson, C., Žagar, N., Vasylyevych, S., Elvidge, S., McCaffrey, A., Prikryl, P.,
769 Reid, B., Wood, A., and Jayachandran, P. T.: Global Propagation of Ionospheric Disturbances
770 Associated With the 2022 Tonga Volcanic Eruption, *Geophysical Research Letters*, 49(7), p.
771 e2022GL098158, doi: <https://doi.org/10.1029/2022GL098158>, 2022.
- 772 Themens, D. R., Jayachandran, P. T. and Langley, R. B.: The nature of GPS differential receiver
773 bias variability: An examination in the polar cap region, *Journal of Geophysical Research: Space*
774 *Physics*, 120(9), pp. 8155–8175, doi: <https://doi.org/10.1002/2015JA021639>, 2015.
- 775 Tsurutani, B. T., and Gonzalez, W. D.: 1987 The cause of high-intensity long-duration
776 continuous AE activity (HILDCAAs): Interplanetary Alfvén wave trains, *Planet. Space*
777 *Sci.*, 35(4), 405–412, doi:10.1016/0032-0633(87)90097-3, 1987
- 778 Tsurutani, B. T., Gould, T., Goldstein, B. E., Gonzalez, W. D., and Sugiura, M.: Interplanetary
779 Alfvén waves and auroral (substorm) activity: Imp 8, *J. Geophys. Res.*, 95(A3), 2241–2252,
780 doi:10.1029/ja095ia03p02241, 1990.
- 781 Tsurutani, B. T., Gonzalez, W. D., Gonzalez, A. L. C., Tang, F., Arballo, J. K., and Okada, M.:
782 Interplanetary origin of geomagnetic activity in the declining phase of the solar cycle, *J.*
783 *Geophys. Res. Space Phys.*, 100(A11), 21717–21733, doi:10.1029/95ja01476, 1995.
- 784 Tsurutani, B. T., et al.: Corotating solar wind streams and recurrent geomagnetic activity: A
785 review, *J. Geophys. Res.*, 111, A07S01, doi:[10.1029/2005JA011273](https://doi.org/10.1029/2005JA011273), 2006.



786

787 Uccellini, L. W. and Koch, S. E.: The Synoptic Setting and Possible Energy Sources for
788 Mesoscale Wave Disturbances, *Monthly Weather Review*, 115(3), pp. 721–729, doi:
789 [https://doi.org/10.1175/1520-0493\(1987\)115<0721:TSSAPE>2.0.CO;2](https://doi.org/10.1175/1520-0493(1987)115<0721:TSSAPE>2.0.CO;2), 1987.

790 Vadas, S. L. and Nicolls, M. J.: Using PFISR measurements and gravity wave dissipative
791 theory to determine the neutral thermospheric winds, *Geophys. Res. Lett.*, 35, L02105,
792 doi:[10.1029/2007GL031522](https://doi.org/10.1029/2007GL031522), 2008.

793 Vadas, S. L. and Azeem, I.: Concentric secondary gravity waves in the thermosphere and
794 ionosphere over the continental United States on March 25–26, 2015 from deep Convection.
795 *Journal of Geophysical Research: Space Physics*, 126, e2020JA028275, [https://](https://doi.org/10.1029/2020JA028275)
796 doi.org/10.1029/2020JA028275

797 Waldock, J. A. and Jones, T. B. (1987) Source regions of medium scale travelling ionospheric
798 disturbances observed at mid-latitudes, *Journal of Atmospheric and Terrestrial Physics*, 49(2),
799 pp. 105–114. doi: [https://doi.org/10.1016/0021-9169\(87\)90044-4](https://doi.org/10.1016/0021-9169(87)90044-4), 2021.

800 Williams, P. J. S., Viridi, T. S., Lewis, R. V., Lester, M., Rodger, A. S., McCrea, I. W., and
801 Freeman, K. S. C.: Worldwide atmospheric gravity-wave study in the European sector 1985–
802 1990, *Journal of Atmospheric and Terrestrial Physics*, 55(4–5), pp. 683–696, doi: 10.1016/0021-
803 9169(93)90014-P, 1993.

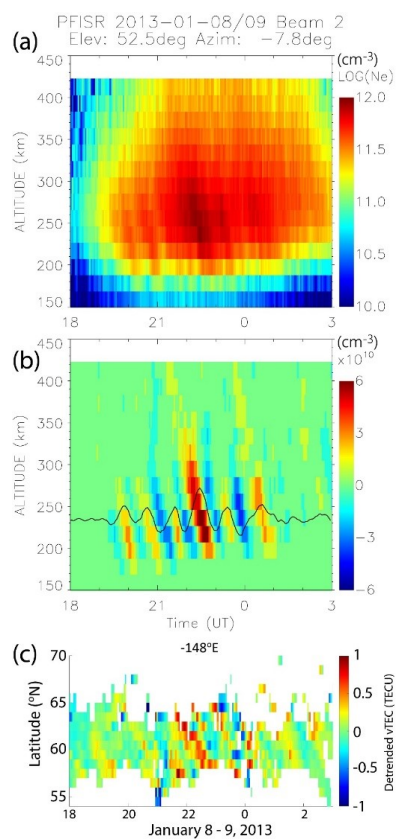
804 Yang, Y.-H., Chao, J.-K. and Lee, L.-C.: On the Walén Relation for Alfvénic Fluctuations in
805 Interplanetary Space, *The Astrophysical Journal*, 904(2), p. 195, doi: 10.3847/1538-4357/abf55,
806 2020.

807 Yu, Y., Wang, W. and Hickey, M. P.: Ionospheric signatures of gravity waves produced by the
808 2004 Sumatra and 2011 Tohoku tsunamis: A modeling study, *Journal of Geophysical Research:*
809 *Space Physics*, 122(1), pp. 1146–1162, doi: <https://doi.org/10.1002/2016JA023116>, 2017.

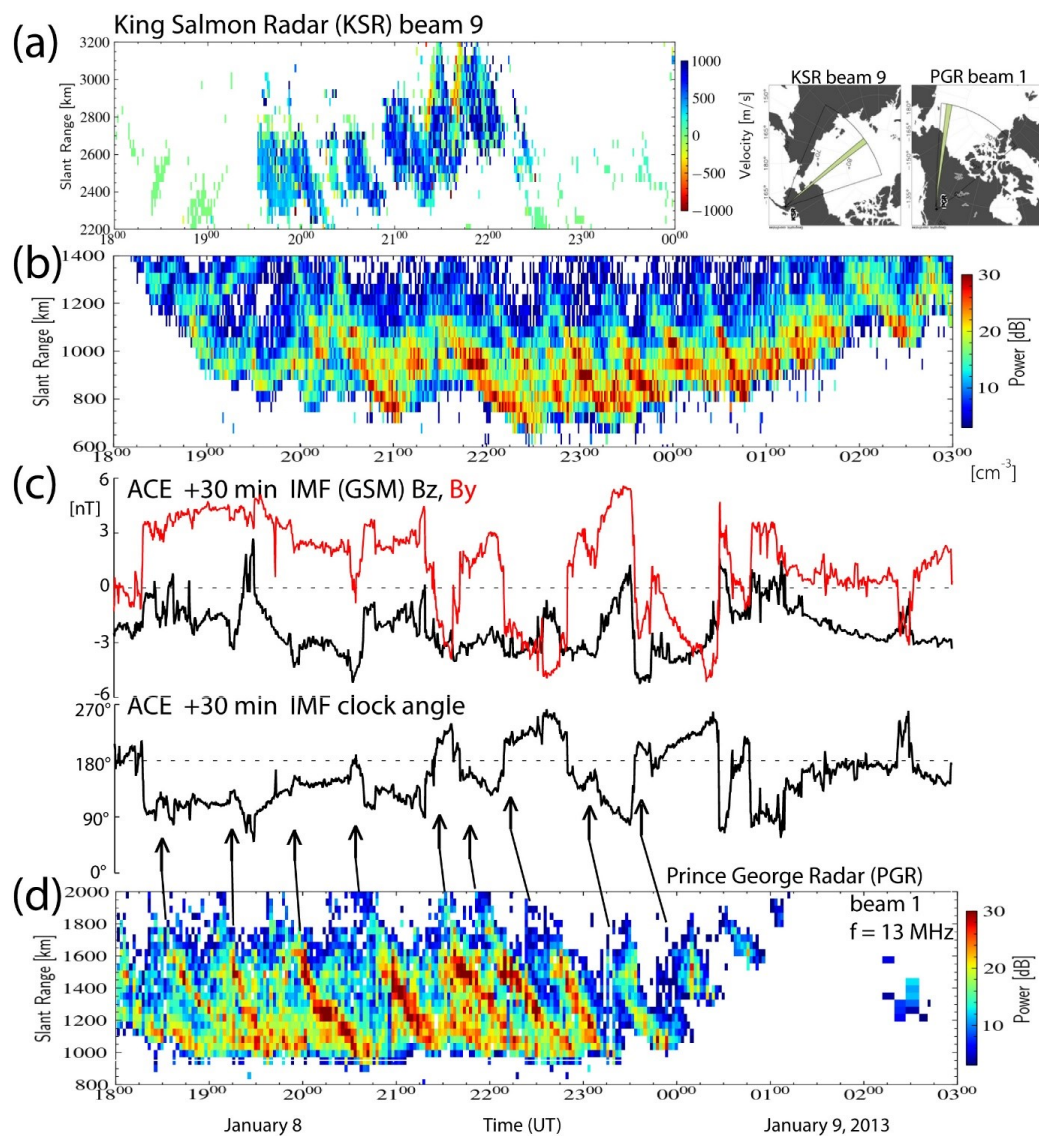
810 Zhang, S.-R., Erickson, P. J., Goncharenko, L. P., Coster, A. J., Rideout, W., and Vierinen, J.:
811 Ionospheric Bow Waves and Perturbations Induced by the 21 August 2017 Solar Eclipse,
812 *Geophysical Research Letters*, 44(24), pp. 12,12-67,73, doi:
813 <https://doi.org/10.1002/2017GL076054>, 2017.

814 **Figures**

815

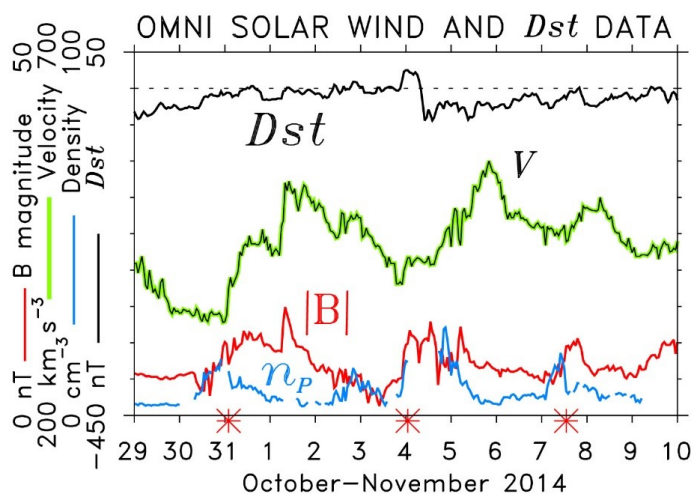


816
817 **Figure 1:** (a) Ionospheric density observed by the PFISR radar beam 2 and (b) detrended using a
818 33-point wide Savitzky-Golay filter. (c) The detrended GNSS vTEC mapped at latitude bins
819 along the longitude of PFISR.

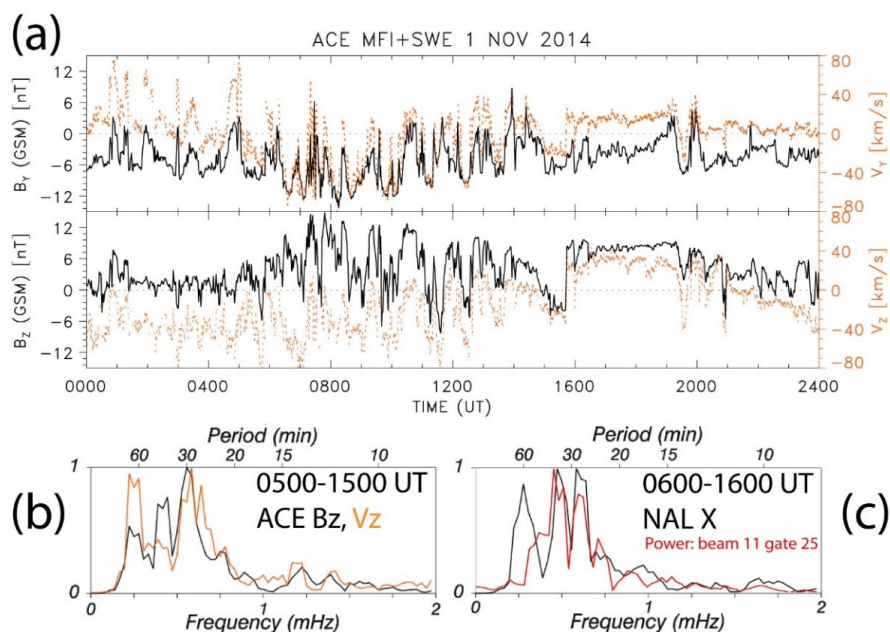


820
821
822
823
824
825
826
827

Figure 2: (a) The line-of-sight velocities and (b) the sea scatter power as a function of the slant range observed by the KSR radar beam 9. (c) Ionospheric density observed by the PFISR radar beam 2 detrended using a 15-point wide Savitzky-Golay filter. (d) The ground scatter power observed by the PGR radar beam 1. The time-shifted time series of the IMF (B_z , B_y) clock angle observed by ACE spacecraft is shown. The arrows indicate southward turning of the IMF.



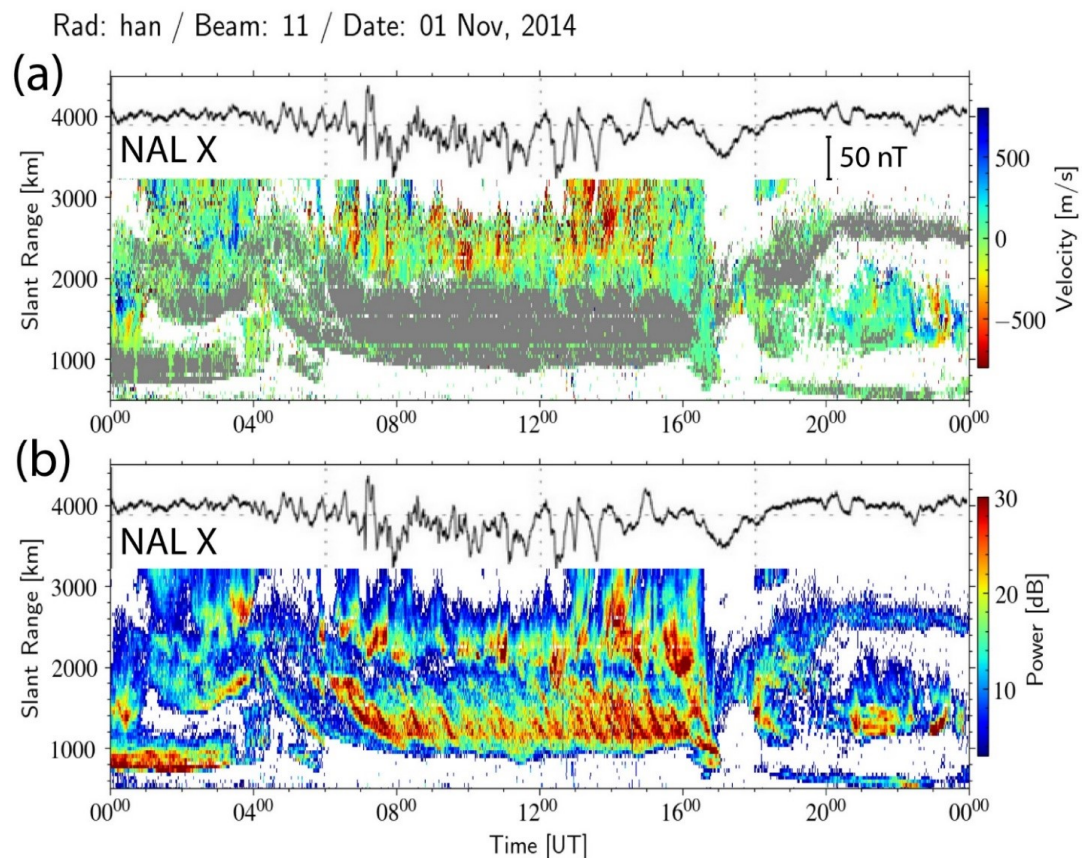
828
 829 **Figure 3:** The OMNI solar wind velocity V , magnetic field magnitude $|B|$, and proton density n_p
 830 showing three HSS/CIRs on October 31, November 4 and 7 are marked by red asterisks at the
 831 time axis. The ring current Dst index is also shown.
 832



833
 834 **Figure 4:** (a) The components of the magnetic field and solar wind velocity observed by ACE,
 835 (b) the FFT spectrum of the detrended time series of IMF B_z and solar velocity V_z , and (c) the
 836 FFT spectrum of the time series of the X-component of ground magnetic field perturbations in
 837 Ny Ålesund (NAL) and the Hankasalmi radar ground scatter power (beam 11, gate 25, slant
 838 range 1305 km; 06:50-16:50 UT).

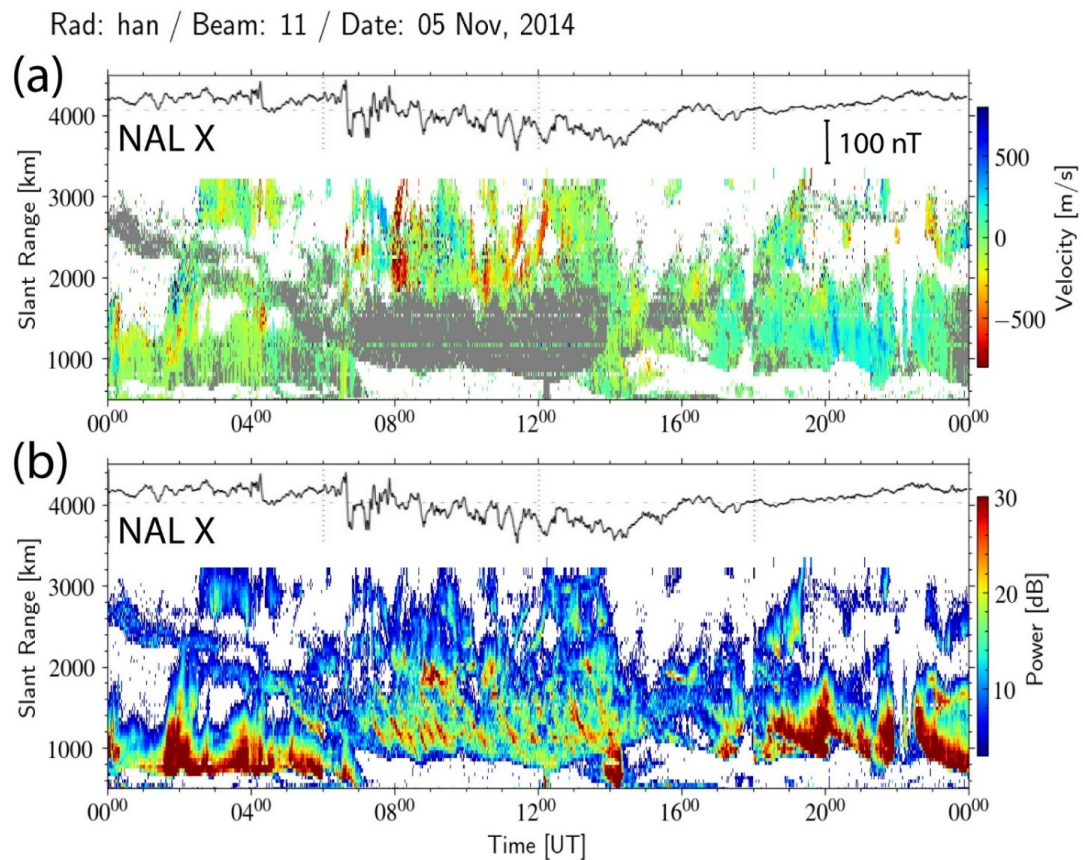


839



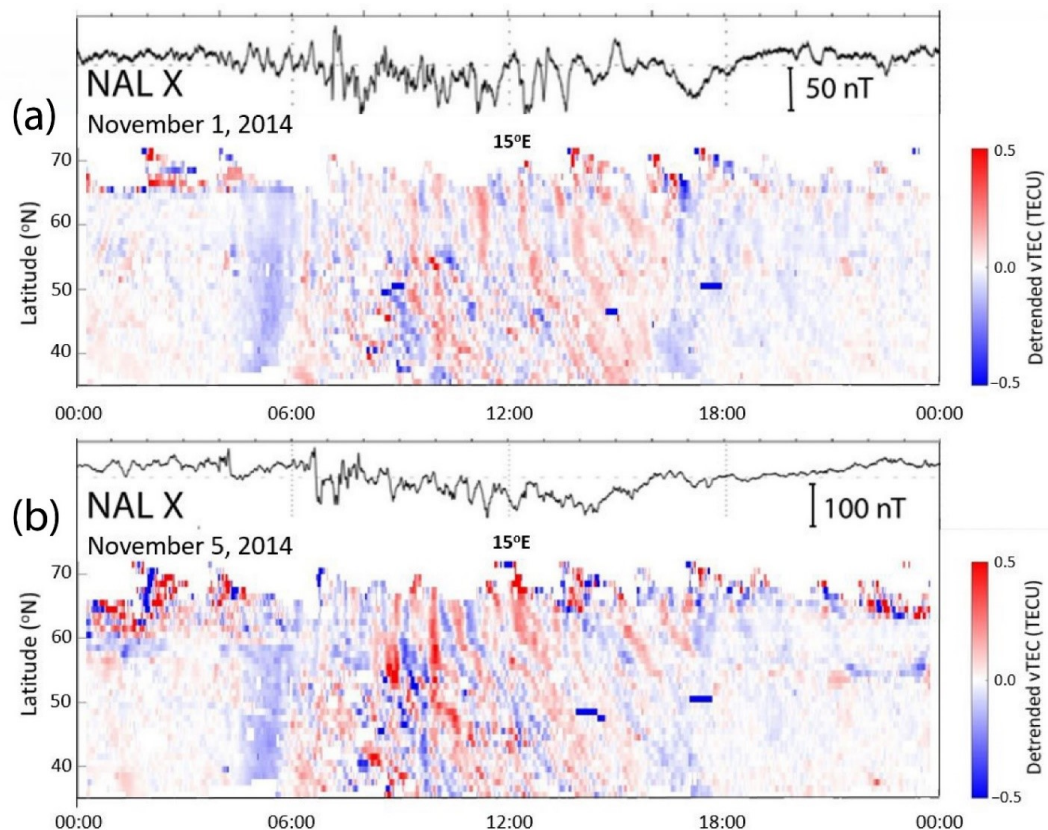
840
841
842
843
844
845
846

Figure 5: (a) The line-of-sight (LoS) velocity and (b) the radar scatter power (ground scatter power shown in grey color in the velocity plot) observed by the Hankasalmi radar beam 11 on November 1, 2014. The X-component of the ground magnetic field perturbations in Ny Ålesund (NAL) is superposed representing the fluctuations of ionospheric currents modulated by solar wind Alfvén waves.

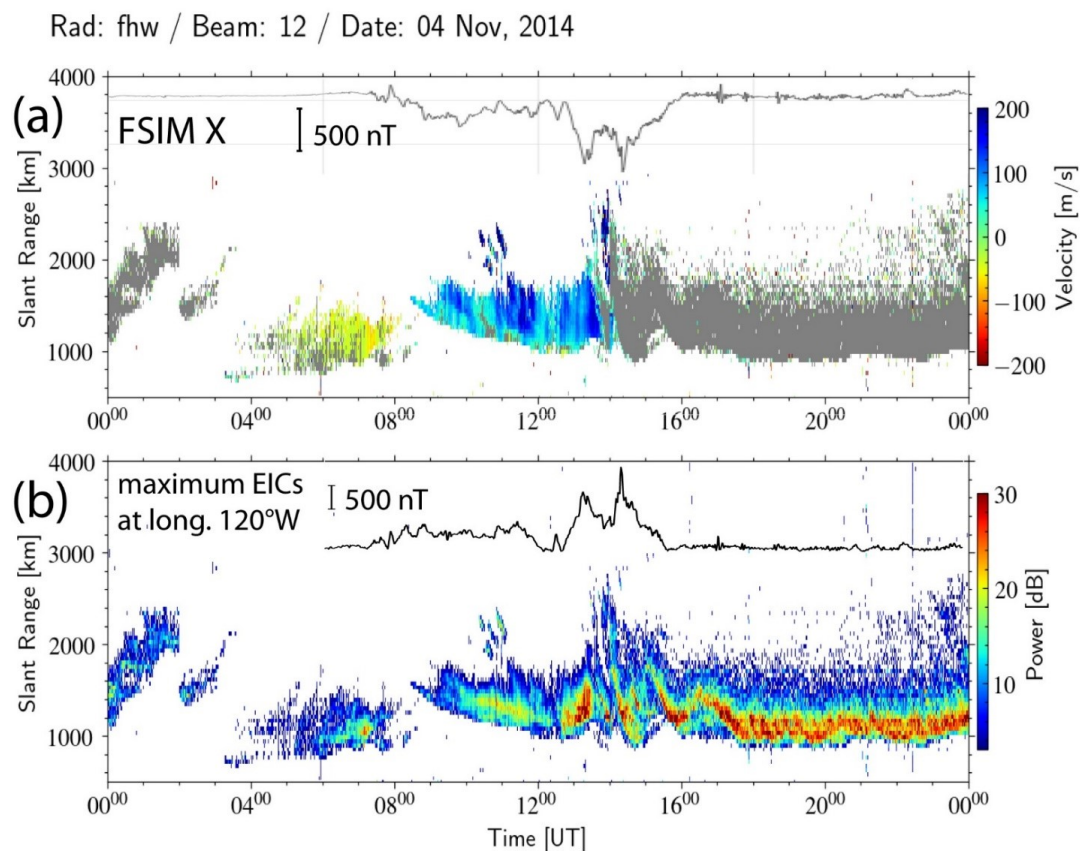


847
848
849

Figure 6: The same as Fig. 5 but for November 5, 2014.

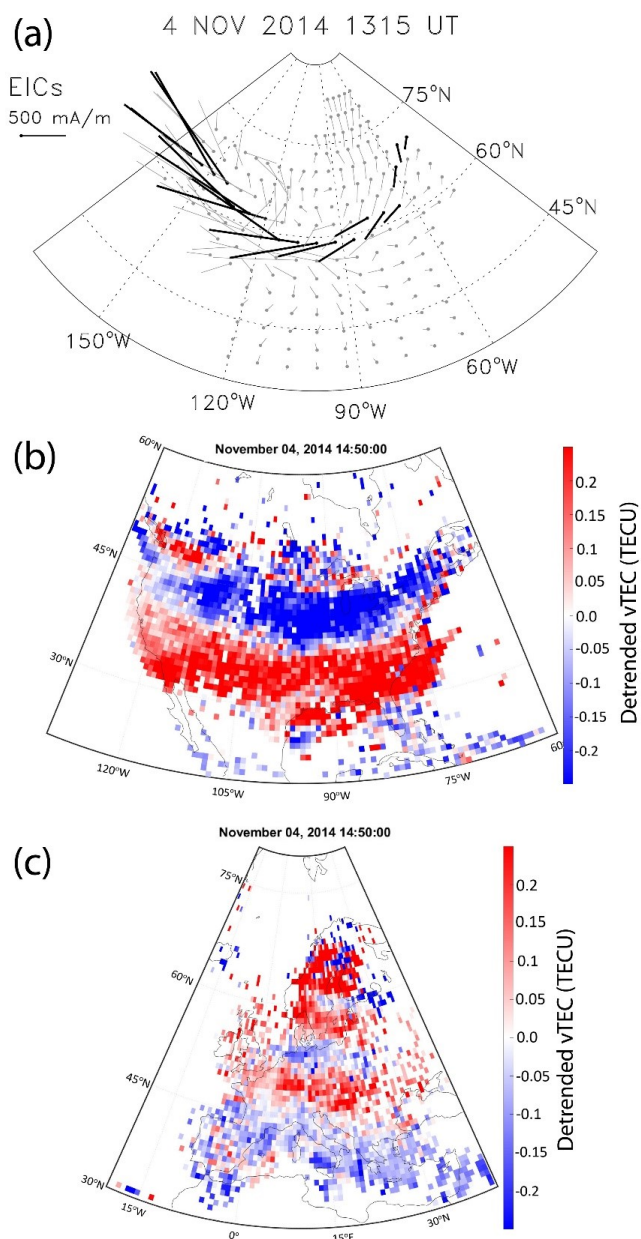


850
851 **Figure 7:** The detrended vTEC mapped along longitude of 15°E on (a) November 1 and (b)
852 November 5, 2014. The X-component of the ground magnetic field perturbations in Ny Ålesund
853 (NAL) is superposed.
854



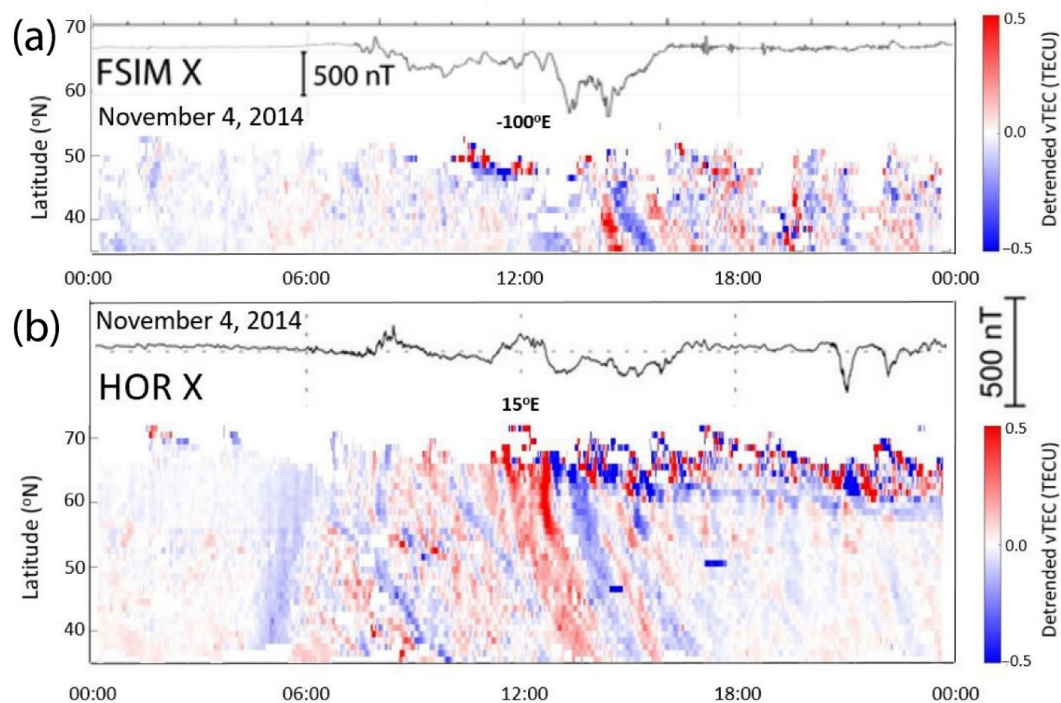
855
856
857
858
859
860

Figure 8: (a) The line-of-sight (LoS) velocity and (b) the radar scatter power (ground scatter power shown in grey color in the velocity plot) observed by the Fort Hays West radar beam 12 on November 4, 2014. The X-component of the ground magnetic field perturbations in Fort Simpson (FSIM) and the maximum EICs at longitude 120°W are superposed.

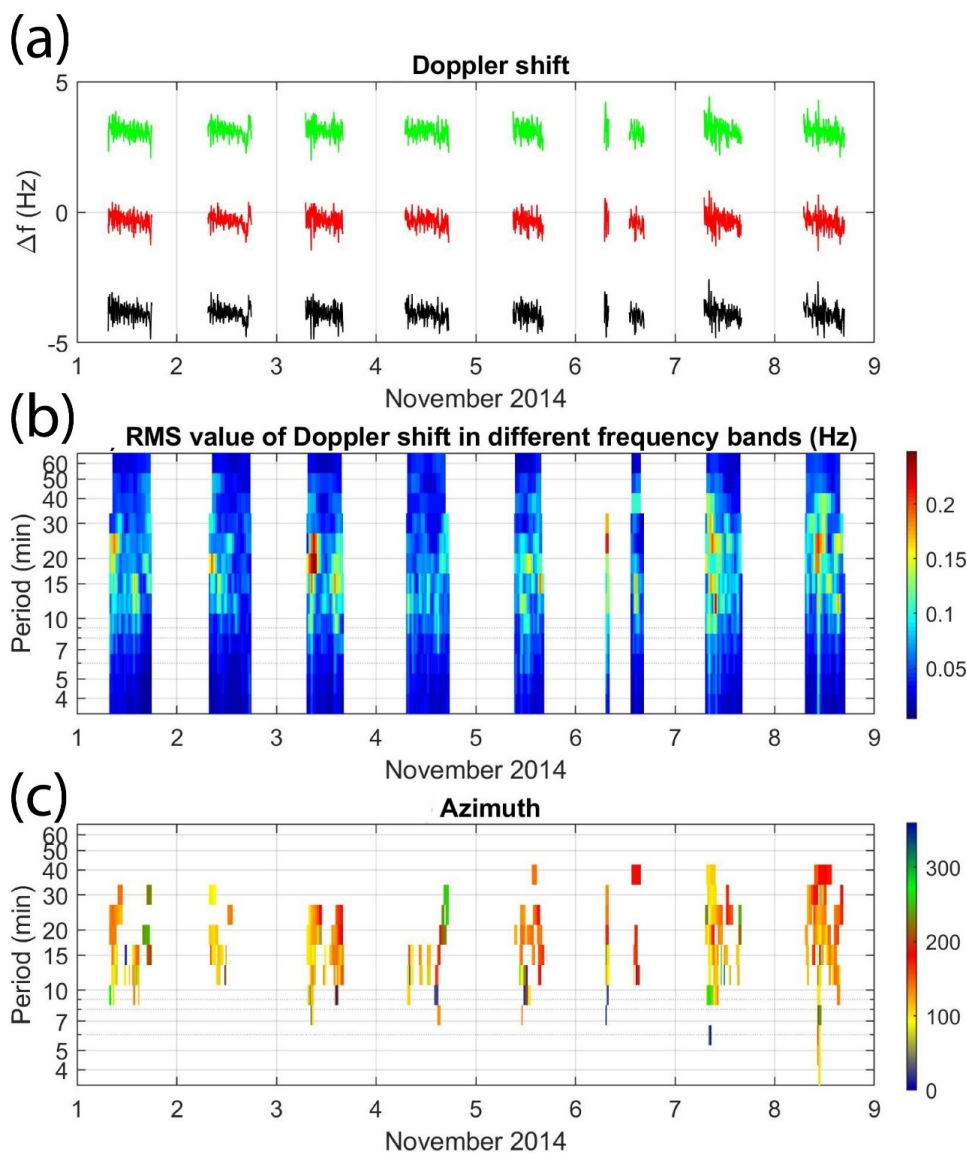


861
862
863
864

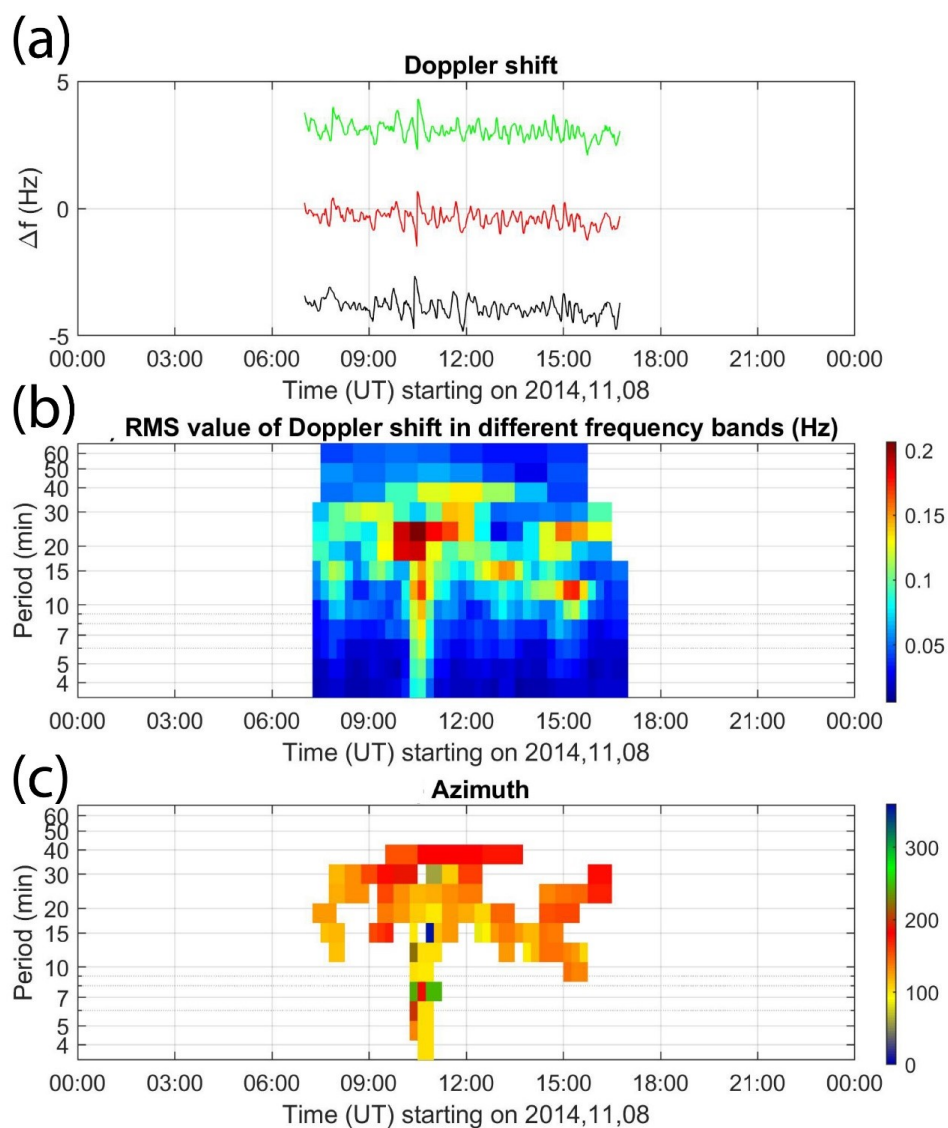
Figure 9: (a) The intensification of the westward electrojet over North America, and the detrended vTEC maps over (b) North America and (c) Europe.



865
866 **Figure 10:** The detrended vTEC mapped along longitude of (a) 100°W and (b) 15°E on
867 November 4, 2014. The X-component of the ground magnetic field in Fort Simpson (FSIM) and
868 Hornsund (HOR) are superposed.
869

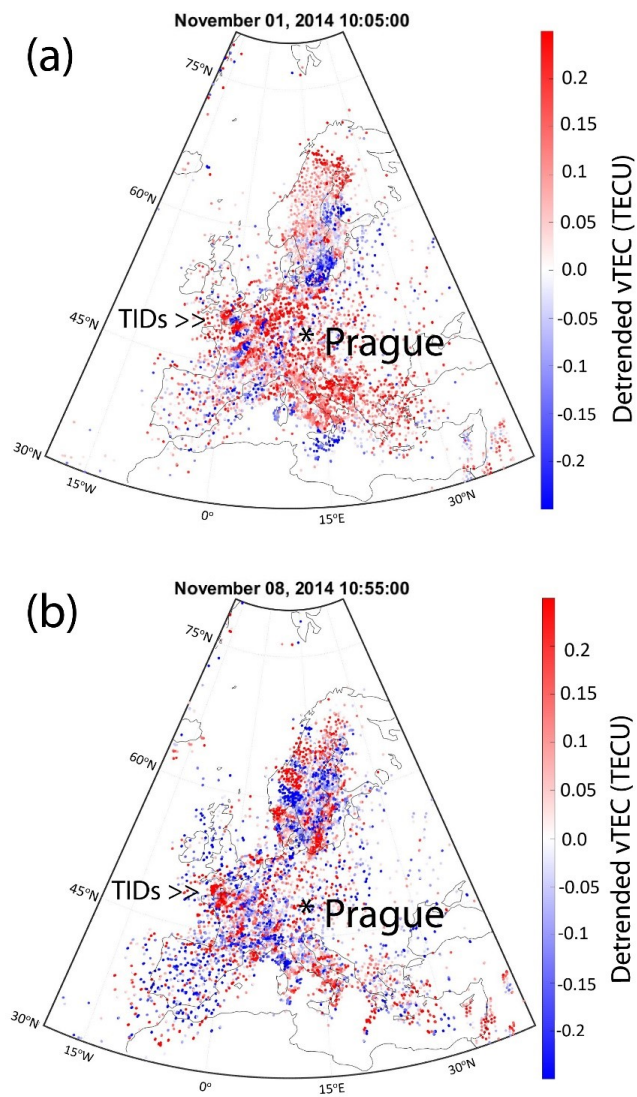


870
871 **Figure 11:** (a) Doppler shift frequencies of spectral density maxima for individual transmitter-
872 receiver pairs (including artificial offsets) from X to Y. (b) Dynamic spectra (periodograms) of
873 Doppler shift signals and (c) the propagation azimuth of waves, displayed as function of period
874 and time for November 1-8, 2014.
875



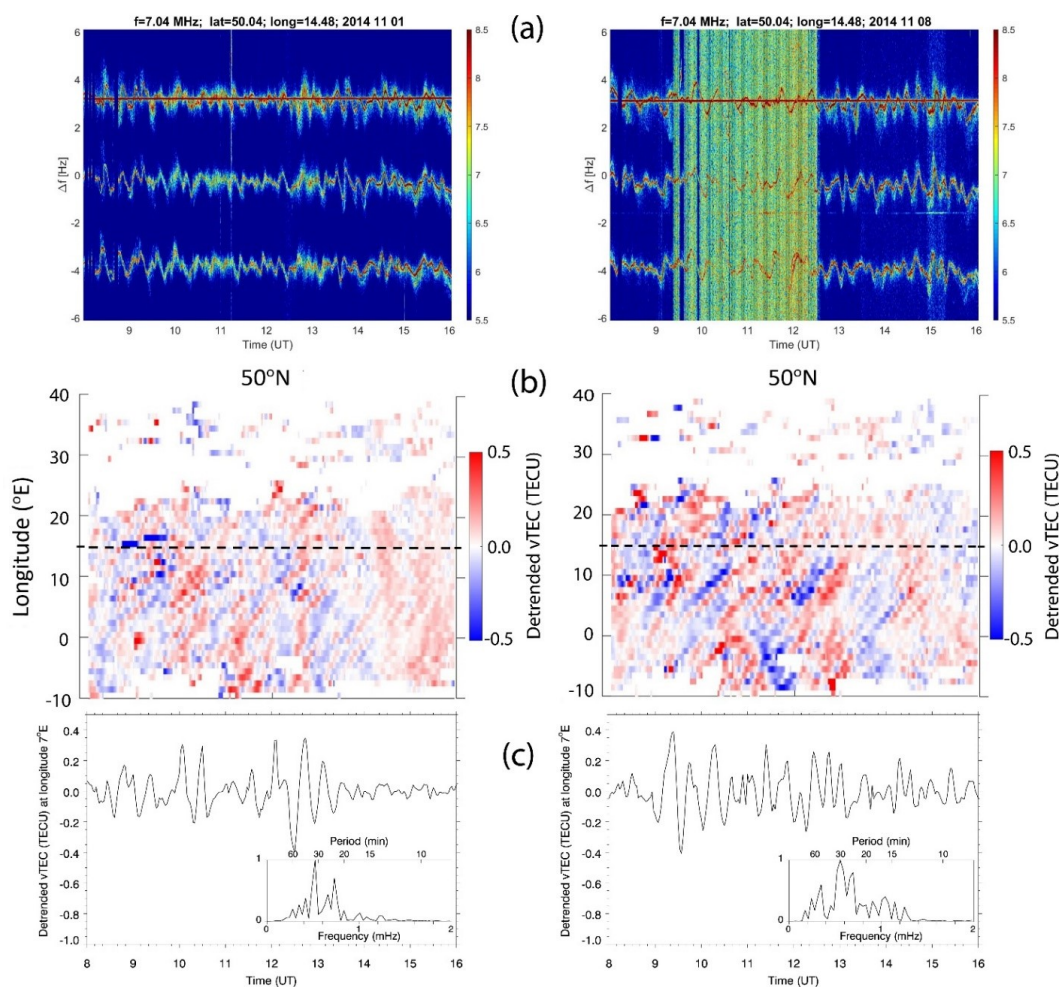
876
877
878

Figure 12: The same as Fig. 11 but expanded for November 8, 2014.



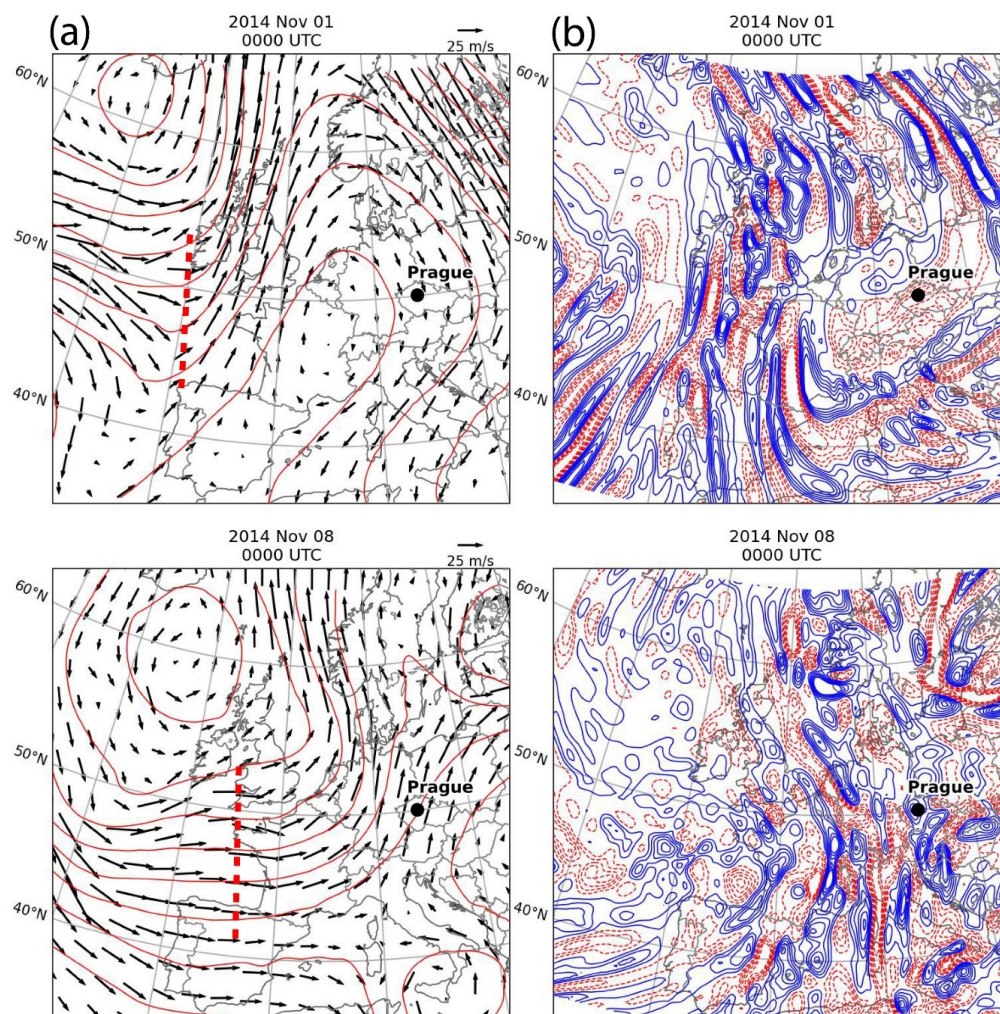
879
880
881

Figure 13: The detrended vTEC maps on (a) November 1 and (b) November 8, 2014.



882
883
884
885
886
887

Figure 14: (a) The Doppler shift spectrogram recorded at frequency 7.04 MHz on November 1 and 8, 2014. (b) The detrended vTEC mapped along latitude of 50°N. The dashed line shows the longitude of Prague. (c) The detrended vTEC time series at longitude of 7°E and the normalized FFT spectra.



888
889 **Figure 15:** (a) The ERA5 geopotential height (red contours at intervals of 100 m), horizontal
890 winds (m/s) at 300-hPa level, with a probable source region of gravity waves indicated by red
891 dashed line. (b) The ERA5 divergence (positive in solid blue line) of the horizontal wind at 150-
892 hPa level, on November 1 and November 8, 2014.
893
894